PHYSICAL REVIEW D **96,** 044028 (2017)

Waveform model for an eccentric binary black hole based on the effective-one-body-numerical-relativity formalism

Zhoujian Cao[1,2,*] and Wen-Biao Han[3,4]

[1]*Department of Astronomy, Beijing Normal University, Beijing 100875, China*
[2]*Institute of Applied Mathematics, Academy of Mathematics and Systems Science, Chinese Academy of Sciences, Beijing 100190, China*
[3]*Shanghai Astronomical Observatory, 80 Nandan Road, Shanghai 200030, People's Republic of China*
[4]*School of Astronomy and Space Science, University of Chinese Academy of Sciences, Beijing 100049, China*

(Received 6 April 2017; published 23 August 2017)

Binary black hole systems are among the most important sources for gravitational wave detection. They are also good objects for theoretical research for general relativity. A gravitational waveform template is important to data analysis. An effective-one-body-numerical-relativity (EOBNR) model has played an essential role in the LIGO data analysis. For future space-based gravitational wave detection, many binary systems will admit a somewhat orbit eccentricity. At the same time, the eccentric binary is also an interesting topic for theoretical study in general relativity. In this paper, we construct the first eccentric binary waveform model based on an effective-one-body-numerical-relativity framework. Our basic assumption in the model construction is that the involved eccentricity is small. We have compared our eccentric EOBNR model to the circular one used in the LIGO data analysis. We have also tested our eccentric EOBNR model against another recently proposed eccentric binary waveform model; against numerical relativity simulation results; and against perturbation approximation results for extreme mass ratio binary systems. Compared to numerical relativity simulations with an eccentricity as large as about 0.2, the overlap factor for our eccentric EOBNR model is better than 0.98 for all tested cases, including spinless binary and spinning binary, equal mass binary, and unequal mass binary. Hopefully, our eccentric model can be the starting point to develop a faithful template for future space-based gravitational wave detectors.

DOI: 10.1103/PhysRevD.96.044028

I. INTRODUCTION

The direct detection of gravitational waves (GW) has been announced recently by LIGO [1–3], which opens a brand new window to the Universe-gravitational wave astronomy. The success of LIGO is based on both the tremendous development of experimental technology and the improvement of theoretical research in the past decades. A matched filtering data analysis technique is very important to gravitational wave detection. As GW150914, GW151226, and GW170104 have witnessed, the matched filtering technique has improved the data quality and/or even made the noisy data detectable. Regarding GW150914 and GW170104, we are somewhat lucky. The signal is so strong that the matched filtering data analysis technology is not necessary to catch the signal, although the matched filtering data analysis can strongly improve the signal to noise ratio (SNR) and confidence level. Regarding GW151226, the signal is much weaker than that of GW150914 and GW170104. Without the matched filtering data analysis technology, the signal is completely invisible. In contrast, the matched filtering data analysis technology digs out the signal from the stronger noise with a SNR 13 and a confidence level 5σ. GW151226 is a good example showing that the detection of the GW is the result of a combination of experimental achievement and theoretical research progress [4].

In order to make the matched filtering technique work, the gravitational waveform template is essential [4]. And the template strongly depends on the specific theoretical model of the GW source. Currently, there are two theoretical models which are ready for gravitational wave data analysis. They are an effective-one-body-numerical-relativity (EOBNR) model [5] and IMRPhenom model [6]. For example, all of GW150914, GW151226 and GW170104 depends strongly upon these two models.

The EOBNR model [7] is a combination of an effective-one-body theory of post-Newtonian approximation and numerical relativity. About the template bank of the binary black hole gravitational waveform, the related parameters are divided into intrinsic ones and extrinsic ones. The EOBNR model needs only to be concerned about the intrinsic parameters, including the total mass of the binary black hole M, the mass ratio $q \equiv \frac{m_1}{m_2} \geq 1$, the spins of the two black holes $\vec{S}_{1,2}$, and the eccentricity of the orbit e. The extrinsic parameters, including the luminosity distance D, the source

*zjcao@amt.ac.cn

location (θ, ϕ), the configuration of the orbit with respect to the sight direction (ι, β), the reaching time of the signal t_0, the initial phase ϕ_0, and the polarization angle with respect to the detector ψ, can be straightforwardly involved when we construct the template bank from EOBNR model.

To the quasicircular $e = 0$ and nonprecession ($\vec{S}_{1,2}$ perpendicular to the orbit plane) binary black hole systems with a mass ratio $q \in (1, \frac{20}{1})$, the EOBNR model has done a quite good job [5]. (Note that the author in [8] mentioned the EOBNR model is valid for a mass ratio range $1 < q < 100$ and a spin range $-1 < \chi < 0.99$. But as pointed out by [9–12], the current EOBNR model can at most be calibrated to a numerical relativity only for the range $1 < q < 20$ and $-0.85 < \chi < 0.85$.) Regarding the precession binaries, a primary development of EOBNR model is available [13]. Very recently, we have done an initial investigation to extend the EOBNR model to include a gravitational wave memory in Ref. [14]. As to the mass ratio, there is no essential difficulty to extend the EOBNR model to cover a larger parameter range. But the current simulation power of numerical relativity limits such a development [15]. In principle, if only the relevant numerical relativity results are available, the EOBNR model can be calibrated to involve the mass ratio. Regarding the eccentricity, the situation is different. Until now, the EOBNR model only worked for the $e = 0$ case. Reference [16] touched on this problem, but the authors only considered the energy flux while they left the relevant gravitational waveform alone. Although the EOBNR model admits the kinds of limitations as described above, it provides a framework which makes it possible to extend the EOBNR model to treat these limitations. Recently, the authors in [17] have extended EOB framework to a scalar-tensor theory. Hopefully, ones can treat the gravitational waveform template for different gravitational theories [18] within one uniform framework, the EOBNR model, in the future.

Because of the circularization effect of gravitational radiation [19], one may expect that the binary black hole systems are always near circular when they enter the LIGO frequency band. But recent investigations show that it is not absolutely true. The study of the galactic cluster M22 indicate that about 20% of the binary black hole (BBH) mergers in globular clusters will have eccentricities larger than 0.1 when they first enter the advanced LIGO band at 10 Hz [20] and that ∼10% may have eccentricities $e \sim 1$ [21]. Furthermore, a fraction of galactic field binaries may retain a significant eccentricity prior to the merger event [22]. BBHs formed in the vicinity of supermassive black holes (BH) may also merge with significant residual eccentricities [23]. For space-based detectors such as eLISA [24], LISA [25,26], Taiji [27], and Tianqin [28], the orbit of the involved binary black hole systems may be highly eccentric due to recent perturbations by other orbiting objects [29,30]. Recently, there are many authors that care about the binary black hole systems with an eccentric orbit with regards to gravitational wave detection [31–34].

Assuming a low eccentricity, the authors of [31] extended a low order PN waveform model in a frequency domain to include the eccentricity. They called the corresponding model a postcircular (PC) model. Later, the authors of [32] improved the PC model to an EPC (enhanced postcircular) model which recovers the TaylorF2 model when the eccentricity vanishes. The EPC model is a phenomenological extension of the PC model. Its overall PN order is 3.5. Some numerical relativity simulations have been paid in the past to the eccentric binary black hole systems [35–37]. Along with the numerical relativity results, the x model was proposed in [36]. The x model is a low order post-Newtonian (PN) model. Recently, this model was improved to include inspiral, merger, and ringdown phases, and higher PN order terms for a vanishing eccentricity part were included. This model was called the ax model by the authors of [34]. All these models are valid for any mass ratio.

Regarding the large mass ratio binary black hole systems, one may look to the binary system as a perturbation of the big black hole. Then the gravitational wave problem is decomposed into the trajectory problem and the related waveform problem. In [38], one of us investigated the eccentric binary using the Teukolsky equation to treat the waveform problem and combined the conserved EOB dynamics with a numerical energy flux to treat the trajectory [39]. In [38,39], the Teukolsky equation is solved numerically. One can also solve it through some analytical method [40] or post-Newtonian approximation [41]. In [42], the authors used a geodesic equation to treat the eccentric orbit of a large mass ratio binary and used the Teukolsky equation to treat the waveform problem. Interestingly, people have used the method of the geodesic equation and the Teukolsky equation to find that the eccentricity may increase [43,44] instead of always decaying as found through the post-Newtonian approximation [19]. In addition, people used the method of the geodesic equation and the Teukolsky equation to find the interesting transient resonance phenomena [45,46]. When a binary system passes through a transient resonance, the radial frequency and polar frequency become commensurate, and the orbital parameters will show a jump behavior. To our knowledge, the post-Newtonian approximation method can not yet give the eccentricity increase and the transient resonance results. Of course, it is possible that the available post-Newtonian result is not accurate enough to get these two interesting phenomena. But it is also deserving to ask whether these two phenomena imply that the perturbation method breaks down. Ideally, ones may use a numerical relativity simulation to check this problem. But unfortunately, current numerical relativity techniques are far away from investigating this problem due to the huge computational cost for large mass ratio binary systems [15] (see [47]). Hopefully, the effective-one-body-numerical-relativity (EOBNR) model may be used to check this

problem. This is because on the side of almost equal mass cases, the EOBNR framework can be and has been calibrated against numerical relativity; on the side of extreme mass ratio cases, the EOB framework can also be and has also been used to describe the dynamics and the gravitational waveform [48]. So we can expect the EOBNR framework may play a bridge role to connect the numerical relativity result with a large mass ratio problem. In order to realize this kind of investigation, we need a EOBNR model valid for eccentric binary systems, which is absent now. In the current paper, we will go a step further to construct an EOBNR model for eccentric binary systems.

This paper is organized as follows. In the next section, we will describe the extended EOBNR model, including eccentricity. We call our model SEOBNRE (spinning effective-one-body-numerical-relativity model for eccentric binary). This model includes three essential parts, which will be explained in detail, respectively, in the subsections of next section. The involved detailed calculations and long equations are postponed to the Appendixes. Then in Sec. III, we check and test our SEOBNRE model against the quasicircular EOBNR model, against the existing eccentric waveform model–ax model, against the numerical relativity simulation results, and against the Teukolsky equation based waveform model for extreme mass ratio binary systems. Finally, we give a summary and a discussion in Sec. IV. Throughout this paper, we will use the units $c = G = 1$. Regarding the mass of the binary, we always assume $m_1 \geq m_2$.

II. WAVEFORM MODEL FOR ECCENTRIC BINARY BASED ON THE EOBNR MODEL

An effective one body technique is a standard trick to treat the two body problem in the central force situation of classical mechanics, especially for the Newtonian gravity theory [49]. In [50], Buonanno and Damour introduced the seminal idea of an effective-one-body approach for a general relativistic two body problem. The effective-one-body approach needs many inputs from a post-Newtonian approximation, but it is more powerful than a post-Newtonian approximation. Unlike the post-Newtonian approximation, which will diverge before the late inspiral stage of the binary evolution, the effective-one-body approach works until the binary merger. And moreover, it is convenient for the effective-one-body approach to adopt the result of a perturbation method [48]. At the same time, we can also combine the results of the effective-one-body approach and numerical relativity. As done first by Pan and his coworkers in [7], such combination gives the effective-one-body numerical relativity (EOBNR) model. Currently, the most advanced EOBNR model is the SEOBNR, which includes version 1 [51], version 2 [5], and version 3 [3,52,53]. SEOBNR is valid only for a quasicircular orbit and black hole spin perpendicular to the orbital plane, which means the precession is not presented. In this paper, we will extend the SEOBNR model to treat the eccentric orbit.

The EOB approach includes three building parts: (1) a description of the conservative part of the dynamics of two compact bodies, which is represented by a Hamiltonian; (2) an expression for the radiation-reaction force, which is added to the conservative Hamiltonian equations of motion; and (3) a description of the asymptotic gravitational waveform emitted by the binary system. The part 1 is independent of the character of the involved orbit. In other words, the part 1 is valid no matter whether the orbit is circular or eccentric. In the current paper, we adopt the result from the SEOBNRv1 model, which will be summarized in the following. Regarding parts 2 and 3, the current SEOBNRv1 model is not valid to an eccentric orbit. We will extend these two parts in the current work. For convenience, we will refer to our model SEOBNRE, where the last letter E represents eccentricity.

A. Conservative part for SEOBNRE model

The conservative part for the SEOBNRE model is the same to that of SEOBNRv1 [51]. But the related equations are distributed in different papers. For convenience, we give a summary here.

The basic idea of the EOB approach is reducing the conservative dynamics of the two body problem in general relativity to a geodesic motion (more precisely, the Mathisson-Papapetrou-Dixon equation [54]) on the top of a reduced spacetime, which corresponds to the reduced one body. Roughly, the reduced spacetime is a deformed Kerr black hole with the metric form [55]

$$ds^2 = g_{tt}dt^2 + g_{rr}dr^2 + g_{\theta\theta}d\theta^2 + g_{\phi\phi}d\phi^2 + 2g_{t\phi}dtd\phi, \quad (1)$$

$$g^{tt} = -\frac{\Lambda_t}{\Delta_t \Sigma}, \quad (2)$$

$$g^{rr} = \frac{\Delta_r}{\Sigma}, \quad (3)$$

$$g^{\theta\theta} = \frac{1}{\Sigma}, \quad (4)$$

$$g^{\phi\phi} = \frac{1}{\Lambda_t}\left(-\frac{\tilde{\omega}_{fd}^2}{\Delta_t \Sigma} + \frac{\Sigma}{\sin^2\theta}\right), \quad (5)$$

$$g^{t\phi} = -\frac{\tilde{\omega}_{fd}}{\Delta_t \Sigma}, \quad (6)$$

where

$$\Sigma = r^2 + a^2\cos^2\theta, \quad (7)$$

$$\Delta_t = r^2\left(A(u) + \frac{a^2u^2}{M^2}\right), \quad (8)$$

$$\Delta_r = \frac{\Delta_t}{D(u)}, \tag{9}$$

$$\Lambda_t = \bar{\omega}^4 - a^2\Delta_t \sin^2\theta, \tag{10}$$

$$\bar{\omega} \equiv \sqrt{r^2 + a^2}, \tag{11}$$

$$\tilde{\omega}_{fd} = 2Mar + \frac{Ma\eta}{r}(\omega_1^{fd} M^2 + \omega_2^{fd} a^2). \tag{12}$$

We still call the coordinate (t, r, θ, ϕ) used here the Boyer-Lindquist coordinate. Following SEOBNRv1, we set $\omega_1^{fd} = 0$ and $\omega_2^{fd} = 0$. Here, M and a are, respectively, the mass and the Kerr spin parameter of the deformed Kerr black hole

$$M \equiv m_1 + m_2, \tag{13}$$

$$M\vec{a} \equiv \vec{\sigma} \equiv \vec{a}_1 m_1 + \vec{a}_2 m_2, \tag{14}$$

and we have used notation $u \equiv \frac{M}{r}$, and

$$A(u) \equiv 1 - 2u + 2\eta u^3 + \eta\left(\frac{94}{3} - \frac{41}{32}\pi^2\right)u^4, \tag{15}$$

$$D(u) \equiv 1/\{1 + \log[1 + 6\eta u^2 + 2(26 - 3\eta)\eta u^3]\}, \tag{16}$$

where $\eta \equiv \frac{m_1 m_2}{(m_1+m_2)^2}$ is the symmetric mass ratio of the binary with the components mass m_1, m_2 and Kerr parameter $\vec{a}_1$ and $\vec{a}_2$.

Corresponding to the geodesic motion, or to say the Mathisson-Papapetrou-Dixon equations, the Hamiltonian can be written as [51,56]

$$H = M\sqrt{1 + 2\eta\left(\frac{H_{\rm eff}}{M\eta} - 1\right)}, \tag{17}$$

$$H_{\rm eff} = H_{NS} + H_S + H_{SC}. \tag{18}$$

The detailed expressions for the quantities H_{NS}, H_S, and H_{SC} involved in the above Hamiltonian are listed in the Appendix A.

Based on the above given Hamiltonian, we have then the equation of motion with respect to the conservative part as

$$\dot{\vec{r}} = \frac{\partial H}{\partial \vec{p}}, \tag{19}$$

$$\dot{\vec{p}} = -\frac{\partial H}{\partial \vec{r}}. \tag{20}$$

B. Gravitational waveform part for the SEOBNRE model

In the EOBNR framework, the gravitational waveform is described by spin-weighted -2 spherical harmonic modes. These kinds of modes are also extensively used in numerical relativity [57]. In SEOBNRv1, the modes $\ell \in \{2, 3, 4, 5, 6, 7, 8\}$, $m \in [-\ell, \ell]$ are available. Note that only the positive m modes are considered while the negative m modes are produced through relation $h_{\ell m} = (-1)^\ell h^*_{\ell,-m}$ [58]. Here, $*$ means the complex conjugate.

In this work, we only consider the $(\ell, m) = (2, 2)$ mode although other modes can be straightforwardly extended. Our basic idea is decomposing the waveform into a quasicircular part and an eccentric part. The strategy is following [34]. We treat the eccentric part as a perturbation by assuming that the eccentricity is small. Regarding the quasicircular part, we borrow exactly the ones from SEOBNRv1. For convenience, we firstly review this part. Within the EOBNR framework, the waveform is divided into two segments. One is after a merger, which is described with the quasinormal modes of some Kerr black hole. The other is an inspiral-plunge stage, which is described in the factorized form as [58]

$$h^{(C)}_{\ell m} = h^{(N,\epsilon)}_{\ell m} \hat{S}^{(\epsilon)}_{\rm eff} T_{\ell m} e^{i\delta_{\ell m}} (\rho_{\ell m})^\ell N_{\ell m}, \tag{21}$$

$$h^{(N,\epsilon)}_{\ell m} = \frac{M\eta}{R} n^{(\epsilon)}_{\ell m} c_{\ell+\epsilon} V_\Phi^\ell Y^{\ell-\epsilon,-m}\left(\frac{\pi}{2}, \Phi\right), \tag{22}$$

where R is the distance to the source; Φ is the orbital phase; $Y^{\ell m}(\Theta, \Phi)$ are the scalar spherical harmonics. Particularly for the (2,2) mode, we have [51,58,59]

$$\epsilon = 0, \tag{23}$$

$$V_\Phi^2 = v_\Phi^2, \tag{24}$$

$$\vec{v}_\Phi = \vec{v}_p - \vec{n}(\vec{v}_p \cdot \vec{n}), \qquad \vec{v}_p \equiv \dot{\vec{r}} = \frac{\partial H}{\partial \vec{p}}, \tag{25}$$

$$n^{(0)}_{\ell m} = (im)^\ell \frac{8\pi}{(2\ell+1)!!}\sqrt{\frac{(\ell+1)(\ell+2)}{\ell(\ell-1)}}, \tag{26}$$

$$c_\ell = \left(\frac{m_2}{m_1+m_2}\right)^{\ell-1} + (-1)^\ell \left(\frac{m_1}{m_1+m_2}\right)^{\ell-1}, \tag{27}$$

$$\hat{S}^{(0)}_{\rm eff} = \frac{H_{\rm eff}}{M\eta}, \tag{28}$$

$$T_{\ell m} = \frac{\Gamma(\ell + 1 - 2im\Omega H)}{\Gamma(\ell+1)} e^{\pi m\Omega H + 2im\Omega H \ln(2m\Omega r_0)}, \tag{29}$$

$$\Omega \equiv v_\Phi^3, r_0 \equiv \frac{2(m_1+m_2)}{\sqrt{e}}, \tag{30}$$

$$N_{\ell m} = \left[1 + \frac{\tilde{p}_r^2}{(r\Omega)^2}\left(a_1^{h_{\ell m}} + \frac{a_2^{h_{\ell m}}}{r} + \frac{a_3^{h_{\ell m}} + a_{3S}^{h_{\ell m}}}{r^{3/2}} + \frac{a_4^{h_{\ell m}}}{r^2} + \frac{a_5^{h_{\ell m}}}{r^{5/2}}\right)\right] \times \exp\left[i\left(\frac{\tilde{p}_r}{r\Omega} b_1^{h_{\ell m}} + \frac{\tilde{p}_r^3}{r\Omega}\left(b_2^{h_{\ell m}} + \frac{b_3^{h_{\ell m}}}{r^{1/2}} + \frac{b_4^{h_{\ell m}}}{r}\right)\right)\right], \tag{31}$$

$$\delta_{22} = \frac{7}{3}\bar{v}^3 + \left(\frac{428}{105}\pi - \frac{4}{3}a\right)\bar{v}^6 + \left(\frac{1712}{315}\pi^2 - \frac{2203}{81}\right)\bar{v}^9 - 24\eta v_\Phi^5 + \frac{20}{63}a v_\Phi^8, \tag{32}$$

$$\begin{aligned}\rho_{22} = 1 &+ \left(\frac{55}{84}\eta - \frac{43}{42}\right)v_\Phi^2 - \frac{2}{3}[\chi_S(1-\eta) + \chi_A\sqrt{1-4\eta}]v_\Phi^3 + \left(\frac{a^2}{2} - \frac{20555}{10584} - \frac{33025}{21168}\eta + \frac{19583}{42336}\eta^2\right)v_\Phi^4 - \frac{34}{21}a v_\Phi^5 \\ &+ \left[\frac{1556919113}{122245200} + \frac{89}{252}a^2 - \frac{48993925}{9779616}\eta - \frac{6292061}{3259872}\eta^2 + \frac{10620745}{39118464}\eta^3 + \frac{41}{192}\eta\pi^2 - \frac{428}{105}\mathrm{eulerlog}_2(v_\Phi^2)\right]v_\Phi^6 \\ &+ \left(\frac{18733}{15876}a + \frac{1}{3}a^3\right)v_\Phi^7 \\ &+ \left[\frac{18353}{21168}a^2 - \frac{1}{8}a^4 - (5.6 + 117.6\eta)\eta - \frac{387216563023}{160190110080} + \frac{9202}{2205}\mathrm{eulerlog}_2(v_\Phi^2)\right]v_\Phi^8 \\ &- \left[\frac{16094530514677}{533967033600} - \frac{439877}{55566}\mathrm{eulerlog}_2(v_\Phi^2)\right]v_\Phi^{10},\end{aligned} \tag{33}$$

$$\chi_S = \frac{a_1/m_1 + a_2/m_2}{2}, \qquad \chi_A = \frac{a_1/m_1 - a_2/m_2}{2}, \tag{34}$$

where we have defined the $\mathrm{eulerlog}_m(v_\Phi^2) \equiv \gamma_E + \ln(2mv_\Phi)$ with $\gamma_E \approx 0.57721566490153286060651209008240 24$ being the Euler constant. In the equation of $N_{\ell m}$, the parameters $a_1^{h_{\ell m}}$, $a_2^{h_{\ell m}}$, $a_3^{h_{\ell m}}$, $b_1^{h_{\ell m}}$, $b_2^{h_{\ell m}}$ are functions of η, and the parameters $a_{3S}^{h_{\ell m}}$, $a_4^{h_{\ell m}}$, $a_5^{h_{\ell m}}$, $b_3^{h_{\ell m}}$, and $b_4^{h_{\ell m}}$ are functions of a and η. Following SEOBNRv1, we construct data tables for $a_i^{h_{\ell m}}$, $a_{3S}^{h_{\ell m}}$, $b_1^{h_{\ell m}}$ and $b_2^{h_{\ell m}}$ based on the numerical relativity results of some specific cases for a and η. Then, we interpolate to get the wanted values for the a and η in question. Then, we solve the conditions (21)–(25) of [51] for $b_3^{h_{\ell m}}$ and $b_4^{h_{\ell m}}$.

For the eccentric part, the post-Newtonian (PN) result is valid until second PN order [60]

$$h^{ij} = 2\eta(Q^{ij} + P^{\frac{1}{2}}Q^{ij} + PQ^{ij} + P^{\frac{3}{2}}Q^{ij} + P^{\frac{3}{2}}Q^{ij}_{\mathrm{tail}}), \tag{35}$$

$$Q^{ij} = 2\left(v_p^i v_p^j - \frac{n^i n^j}{r}\right), \tag{36}$$

$$P^{\frac{1}{2}}Q^{ij} = (m_1 - m_2)\left[\frac{3N_n}{r}(n^i v_p^j + v_p^i n^j - \dot{r} n^i n^j) + N_v\left(\frac{n^i n^j}{r} - 2v_p^i v_p^j\right)\right], \tag{37}$$

$$\begin{aligned}PQ^{ij} = \frac{1}{3}\Bigg\{&(1-3\eta)\left[\frac{N_n^2}{r}\left(\left(3v_p^2 - 15\dot{r}^2 + \frac{7}{r}\right)n^i n^j + 15\dot{r}(n^i v_p^j + v_p^i n^j) - 14 v_p^i v_p^j\right)\right. \\ &\left. + \frac{N_n N_v}{r}(12\dot{r} n^i n^j - 16(n^i v_p^j + v_p^i n^j)) + N_v^2\left(6 v_p^i v_p^j - \frac{2}{r}n^i n^j\right)\right] + \left[3(1-3\eta)v_p^2 - 2\frac{(2-3\eta)}{r}\right]v_p^i v_p^j \\ &+ \frac{2}{r}\dot{r}(5+3\eta)(n^i v_p^j + v_p^i n^j) + \left[3(1-3\eta)\dot{r}^2 - (10+3\eta)v_p^2 + \frac{29}{r}\right]\frac{n^i n^j}{r}\Bigg\},\end{aligned} \tag{38}$$

$$P^{\frac{3}{2}}Q^{ij} = (m_1-m_2)(1-2\eta)\left\{\frac{N_n^3}{r}\left[\frac{5}{4}\left(3v_p^2-7\dot{r}^2+\frac{6}{r}\right)\dot{r}n^in^j-\frac{17}{2}\dot{r}v_p^iv_p^j-\left(21v_p^2-105\dot{r}^2+\frac{44}{r}\right)\frac{n^iv_p^j+v_p^in^j}{12}\right]\right.$$
$$+\frac{1}{4}\frac{N_n^2N_v}{r}\left[58v_p^iv_p^j+\left(45\dot{r}^2-9v_p^2-\frac{28}{r}\right)n^in^j-54\dot{r}(n^iv_p^j+v_p^in^j)\right]+\frac{3}{2}\frac{N_nN_v^2}{r}(5(n^iv_p^j+v_p^in^j)-3\dot{r}n^in^j)$$
$$\left.+\frac{1}{2}N_v^3\left(\frac{n^in^j}{r}-4v_p^iv_p^j\right)\right\}+\frac{\delta m}{12}\frac{N_n}{r}\left\{(n^iv_p^j+v_p^in^j)\left[\dot{r}^2(63+54\eta)-\frac{128-36\eta}{r}+v_p^2(33-18\eta)\right]\right.$$
$$\left.+n^in^j\dot{r}\left[\dot{r}^2(15-90\eta)-v_p^2(63-54\eta)+\frac{242-24\eta}{r}\right]-\dot{r}v_p^iv_p^j(186+24\eta)\right\}$$
$$+(m_1-m_2)N_v\left\{\frac{1}{2}v_p^iv_p^j\left[\frac{3-8\eta}{r}-2v_p^2(1-5\eta)\right]-\frac{n^iv_p^j+v_p^in^j}{2r}\dot{r}(7+4\eta)\right.$$
$$\left.-\frac{n^in^j}{r}\left[\frac{3}{4}(1-2\eta)\dot{r}^2+\frac{1}{3}\frac{26-3\eta}{r}-\frac{1}{4}(7-2\eta)v_p^2\right]\right\}, \tag{39}$$

$$P^{\frac{3}{2}}Q^{ij}_{\rm tail} = 4v_p^5[\pi(\lambda^i\lambda^j-n^in^j)+6\ln v_p(\lambda^in^j+n^i\lambda^j)]. \tag{40}$$

In the above equations, we have used the following notations. $\hat{N}=(\sin\theta\cos\phi,\sin\theta\sin\phi,\cos\phi)$ is the radial direction to the observer. $\hat{p}=(\cos\theta\cos\phi,\cos\theta\sin\phi,-\sin\theta)$ lies along the line of nodes. $\hat{q}=\hat{N}\times\hat{p}$ and more notations include [60,61]

$$N_n=\hat{N}\cdot\vec{n}, \tag{41}$$

$$N_v=\hat{N}\cdot\vec{v_p}, \tag{42}$$

$$\vec{\lambda}=\frac{\vec{v_p}-(\vec{v_p}\cdot\vec{n})\vec{n}}{|\vec{v_p}-(\vec{v_p}\cdot\vec{n})\vec{n}|}. \tag{43}$$

We define the spin-weighted spherical harmonic modes as

$$\epsilon^+_{ij}=\frac{1}{2}(\hat{p}_i\hat{p}_j-\hat{q}_i\hat{q}_j), \tag{44}$$

$$\epsilon^\times_{ij}=\frac{1}{2}(\hat{p}_i\hat{q}_j+\hat{q}_i\hat{p}_j). \tag{45}$$

$$h_+=\epsilon^+_{ij}h^{ij}, \tag{46}$$

$$h_\times=\epsilon^\times_{ij}h^{ij}. \tag{47}$$

$$h=h_+-ih_\times, \tag{48}$$

$$h_{\ell,m}=\int h^{-2}Y^*_{\ell,m}d\Omega. \tag{49}$$

Based on the above results, we express the (2,2) mode as

$$h_{22}=2\eta[\Theta_{ij}(Q^{ij}+P_0Q^{ij}+P^{\frac{3}{2}}Q^{ij}_{\rm tail})+P_n\Theta_{ij}(P^{\frac{1}{2}}_nQ^{ij}+P^{\frac{3}{2}}_nQ^{ij})+P_v\Theta_{ij}(P^{\frac{1}{2}}_vQ^{ij}+P^{\frac{3}{2}}_vQ^{ij})+P_{nn}\Theta_{ij}P_{nn}Q^{ij}$$
$$+P_{nv}\Theta_{ij}P_{nv}Q^{ij}+P_{vv}\Theta_{ij}P_{vv}Q^{ij}+P_{nnn}\Theta_{ij}P^{\frac{3}{2}}_{nnn}Q^{ij}+P_{nnv}\Theta_{ij}P^{\frac{3}{2}}_{nnv}Q^{ij}+P_{nvv}\Theta_{ij}P^{\frac{3}{2}}_{nvv}Q^{ij}$$
$$+P_{vvv}\Theta_{ij}P^{\frac{3}{2}}_{vvv}Q^{ij}]. \tag{50}$$

The involved notations, such Θ_{ij} and $P_n\Theta_{ij}$, are explained one by one in the Appendix B.

We assume the h_{22} in the Eq. (50) includes a quasicircular part corresponding to $h_{22}|_{\dot{r}=0}$ and the left eccentric part. It is straightforward to check that $h_{22}|_{\dot{r}=0}$ is consistent to the Eq. (9.3) of [62]. So we define the eccentric correction as

$$h^{(PNE)}_{22}=h_{22}-h_{22}|_{\dot{r}=0}, \tag{51}$$

where h_{22} means the one given in the Eq. (50). In summary, the inspiral-plunge waveform for SEOBNRE is

$$h^{\rm insp-plun}_{22}=h^{(C)}_{22}+h^{(PNE)}_{22}, \tag{52}$$

where $h^{(C)}_{22}$ is given in Eq. (21).

C. Radiation-reaction force for the SEOBNRE model

We have mentioned the conservative part of the EOB dynamics in Eqs. (19) and (20). But that is only a partial part of the whole EOB dynamics. The left part is related to the radiation-reaction force. Assuming the radiation-reaction force is $\vec{\mathcal{F}}$, then the whole EOB dynamics can be expressed as

$$\dot{\vec{r}} = \frac{\partial H}{\partial \vec{p}}, \tag{53}$$

$$\dot{\vec{p}} = -\frac{\partial H}{\partial \vec{r}} + \vec{\mathcal{F}}. \tag{54}$$

In the SEOBNRv1 model, the radiation-reaction force $\vec{\mathcal{F}}$ is related to the energy flux of the gravitational radiation $\frac{dE}{dt}$ through [51]

$$\vec{\mathcal{F}} = \frac{1}{M\eta\omega_\Phi |\vec{r}\times\vec{p}|}\frac{dE}{dt}\vec{p}, \tag{55}$$

$$\omega_\Phi = \frac{|\vec{r}\times\dot{\vec{r}}|}{r^2}. \tag{56}$$

Here, we need to note the sign of $\frac{dE}{dt}$. Since E here means the energy of the binary system, E decreases due to the gravitational radiation, $\frac{dE}{dt} < 0$. So people sometimes call it dissipation. This corresponds to the SEOBNRv1 code [63], since it treats quasicircular cases without precession, $|\vec{r}\times\vec{p}| \approx \tilde{p}_\phi$, which reduces

$$\vec{\mathcal{F}} = \frac{1}{M\eta\omega_\Phi}\frac{dE}{dt}\frac{\vec{p}}{\tilde{p}_\phi}. \tag{57}$$

Regarding the energy flux $\frac{dE}{dt}$, the SEOBNR model relates it to the gravitational waveform through [59]

$$-\frac{dE}{dt} = \frac{1}{16\pi}\sum_\ell \sum_{m=-\ell}^{\ell} |\dot{h}_{\ell m}|^2. \tag{58}$$

And the more the SEOBNR model assumes the dependence of $h_{\ell m}$ onto time, it is more of an harmonic oscillation. So $\dot{h}_{\ell m} \approx m\Omega h_{\ell m}$ with Ω the orbital frequency of the binary. Then,

$$-\frac{dE}{dt} = \frac{1}{16\pi}\sum_\ell \sum_{m=-\ell}^{\ell} (m\Omega)^2 |h_{\ell m}|^2 \tag{59}$$

$$= \frac{1}{8\pi}\sum_\ell \sum_{m=1}^{\ell} (m\Omega)^2 |h_{\ell m}|^2. \tag{60}$$

Like the EOBNR models, our SEOBNRE model is valid only for spin aligned binary black holes (spin is perpendicular to the orbital plane). In these systems, there is no precession to be involved. Most importantly, these systems admit a plane reflection symmetry with respect to the orbital plane. Because of this symmetry of the corresponding spacetime and the symmetry of the spin-weighted spherical harmonic functions, we have [Eqs. (44)–(46) of [64]]

$$h(t, \pi-\theta, \phi) = h^*(t, \theta, \phi), \tag{61}$$

$${}^{-2}Y_{\ell,-m}(\pi-\theta,\phi) = {}^{-2}Y^*_{\ell m}(\theta,\phi). \tag{62}$$

Here, we have used (θ, ϕ) to represent the spherical coordinate with respect to the gravitational wave source. Consequently, we have $h_{\ell m} = (-1)^\ell h^*_{\ell,-m}$ [58]. In the second equality of the above energy flux equation, the SEOBNR model has taken this relation into consideration and has neglected the "memory" modes $h_{\ell 0}$ [14,65]. We also note that some authors use the relation $h_{\ell m} = (-1)^\ell h^*_{\ell,-m}$ as an assumption in the cases where the plane reflection symmetry breaks down [5,13,52].

In our SEOBNRE model, we follow the steps of the SEOBNRv1 model to construct the radiation reaction force. The only difference is replacing the waveform with our SEOBNRE waveforms (52).

Besides the above method to calculate the energy flux, one may also calculate $\frac{dE}{dt}$ based on a post-Newtonian approximation together with results from the conservative part of the EOBNR model. This is the method taken by the ax model [34]. Similar to the idea we have taken to treat the waveform in the above Sec. II A, we divide the energy flux into two parts which correspond to the circular part and the noncircular correction part. Then, the overall energy flux can be written as

$$\frac{dE}{dt} = \left.\frac{dE}{dt}\right|_{(C)} + \left.\frac{dE}{dt}\right|_{\text{Elip}} - \left.\frac{dE}{dt}\right|_{\text{Elip},\dot{r}=0}. \tag{63}$$

We give the detail calculations for the post-Newtonian energy fluxes including $\frac{dE}{dt}|_{(C)}$ and $\frac{dE}{dt}|_{\text{Elip}}$ for eccentric binary in the Appendix C.

D. Initial data setting for the SEOBNRE dynamics

Within the EOB framework, we solve the dynamical Eqs. (53) and (54), then plug the evolved dynamical variables into the waveform expression (52). But first, we need to setup the initial value for the dynamical variables $(\vec{r}, \vec{p})$. We take two steps to set the initial values. First, we look for the dynamical variable values for a circular orbit (the authors in [66] call it a spherical orbit). Secondly, we adjust the momentum to achieve wanted eccentricity. In this work, we consider binary black holes with a spin perpendicular to the orbital plane. So the dynamics can be described with the test particle moves on the ecliptic plane of the central deformed Kerr geometry [58]. Within the Boyer-Lindquist coordinate, we have $\phi = 0$, $\theta = \frac{\pi}{2}$, $\tilde{p}_\theta = 0$. In order to get r, $\tilde{p}_r$, and $\tilde{p}_\phi$, we follow the Eqs. (4.8) and (4.9) of [66] to solve

$$\frac{dH}{dr} = 0, \tag{64}$$

$$\frac{dH}{d\tilde{p}_\theta} = 0, \tag{65}$$

$$\frac{dH}{d\tilde{p}_\phi} = \omega_0, \tag{66}$$

where $\omega_0 = \frac{\pi}{f_0}$ is the speculated orbital frequency at initial time and the f_0 is the given frequency for a gravitational wave at initial time. Assuming the resulting solution for r is $\hat{r}$, we adjust r through

$$r_0 = \hat{r}/(1+e_0), \tag{67}$$

which means we put the test particle on the periastron of an elliptic orbit with an eccentricity e_0 based on a Newtonian picture [38]. If the approximation of the test particle and the Newtonian picture is not good enough, our initial data setting method can not work well. More sophisticated initial conditions for the eccentric binary black hole system are possible [67]. We leave such investigations to future study.

E. Match the inspiral waveform to the merger-ringdown waveform

Like other EOBNR models, we assume the ringdown waveform can be described by the combination of quasinormal modes as

$$h_{\ell m}^{\text{merger-RD}} = \sum_{n=0}^{N-1} A_{\ell mn} e^{-i\sigma_{\ell mn}(t-t_{\text{match}}^{\ell m})}, \tag{68}$$

where $\sigma_{\ell mn}$ are the complex eigenvalues of the corresponding quasinormal modes for a Kerr black hole, $t_{\text{match}}^{\ell m}$ is the matching time point, and $A_{\ell mn}$ are the combination coefficients for each mode. The same for SEOBNRv1 [63], we take $N = 8$.

In order to determine $\sigma_{\ell mn}$, we need to know the mass and spin of the final Kerr black hole. In principle, the mass and the spin may be affected by the eccentricity. But here we neglect such a dependence on the eccentricity as [34] based on the assumption that the eccentricity is small for the cases considered in current work. We specify the mass and the spin of the final black hole following [68,69]

$$M_{\text{final}} = M[1 + 4(m^0 - 1)\eta + 16 m^1 \eta^2 (\chi_1 + \chi_2)], \tag{69}$$

$$\begin{aligned}
\chi_{\text{final}} &\equiv \frac{a_{\text{final}}}{M_{\text{final}}} = \chi^0 + \eta\chi^0(t_4\chi^0 + t_5\eta + t_0) \\
&\quad + \eta(2\sqrt{3} + t_2\eta + t_3\eta^2), \\
m^0 &= 0.9515, \qquad m^1 = -0.013, \\
q &= \frac{m_1}{m_2}, \qquad \chi^0 = \frac{\chi_1 + \chi_2 q^2}{1+q^2}, \qquad \chi_{1,2} \equiv \frac{a_{1,2}}{m_{1,2}}, \\
t_0 &= -2.8904, \qquad t_2 = -3.5171, \qquad t_3 = 2.5763, \\
t_4 &= -0.1229, \qquad t_5 = 0.4537.
\end{aligned} \tag{70}$$

Note that the above relations are valid only for the spins of the two black holes perpendicular to the orbital plane, which are the cases considered in current work.

Regarding the matching time point $t_{\text{match}}^{\ell m}$, we determine it based on inspiral dynamics as follows. For the inspiral part, we solve the dynamics (53) and (54) until a time point which is called "merger time point" for convenience. The criteria of the "merger time point" is $r < 6M$, and the orbital frequency begins to decrease. Then, we chose the matching time point $t_{\text{match}}^{\ell m}$ corresponding to the time of the peak amplitude of the waveform $h_{\ell m}^{\text{insp-plun}}$.

At last, we determine the coefficients $A_{\ell mn}$ based on the rule that the matching is smooth at $t_{\text{match}}^{\ell m}$ through the first order derivative of the waveform.

III. TEST RESULTS FOR THE SEOBNRE MODEL

In this section, we will compare our SEOBNRE model to several existing waveform results, including the SEOBNR model, ax model, a numerical relativity simulation, and Teukolsky equation results. In addition to the comparison between the waveforms directly, we use an overlap factor to quantify the difference between our SEOBNRE model and these existing waveform results [70]. For two waveforms $h(t)$ and $s(t)$, the overlap factor is defined as

$$\mathcal{O}(h,s) \equiv \frac{\langle h|s\rangle}{\sqrt{\langle h|h\rangle\langle s|s\rangle}}, \tag{71}$$

with the inner product defined as

$$\langle h|s\rangle \equiv 4\text{Re}\int_{f_{\min}}^{f_{\max}} \frac{\tilde{h}(f)\tilde{s}^*(f)}{S_n(f)} df, \tag{72}$$

where $\tilde{}$ means the Fourier transformation, f represents frequency, $S_n(f)$ is the one sided power spectral density of the detector noise, and $(f_{\min}, f_{\max})$ is the frequency range of the detector. As a typical example, we consider an advanced LIGO detector in the following investigations. More specifically, we take the sensitivity of LIGO-Hanford during O1 run as our $S_n(f)$, which was determined from the LSC webpage [71]. Correspondingly, we take $f_{\min} =$ 20 Hz and $f_{\max} = 2000$ Hz. Like other existing waveform models, the total mass M of the binary black hole, the source location (θ, ϕ), the angles between the eccentric orbit and the line direction (ι, β), and the polarization angle ψ are free parameters [33]. But in order to let the waveform fall into the LIGO's frequency band, we choose $M = 20\text{M}_\odot$ as an example to calculate the overlap factor $\mathcal{O}$. Regarding the five angles, values $\theta = \phi = \iota = \beta = \psi = 0$ are taken.

A. Comparison to SEOBNRv1

Firstly, we compare the result of the SEOBNRE model with $e_0 = 0$ against to SEOBNRv1. We consider two

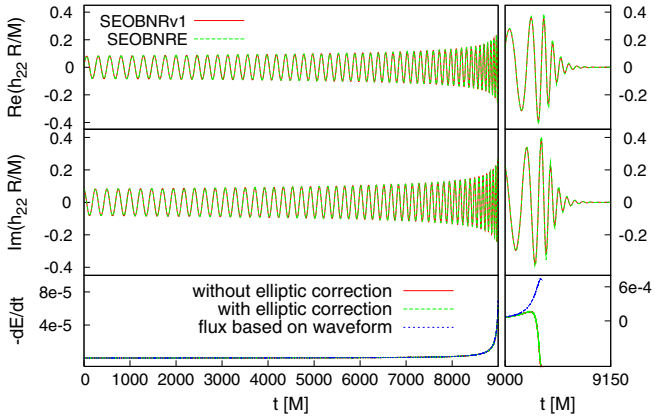

FIG. 1. Test for two identical spinless black holes with an eccentricity $e_0 = 0$. The four top panels are comparison of the $(\ell = 2,\ m = 2)$ mode of the gravitational waveform for SEOBNRE and SEOBNRv1. The bottom two panels are comparison of the energy flux for the one generated with waveform (60), $-\frac{dE}{dt}$ given in (63) and $-\frac{dE}{dt}|_{(C)}$ in (C1). In the plot, the energy flux generated with waveform (60) is marked with "flux based on waveform". The $-\frac{dE}{dt}$ given in (63) is marked with "with elliptic correction". The $-\frac{dE}{dt}|_{(C)}$ in (C1) is marked with "without elliptic correction". The SEOBNRE model is used in the energy flux comparison.

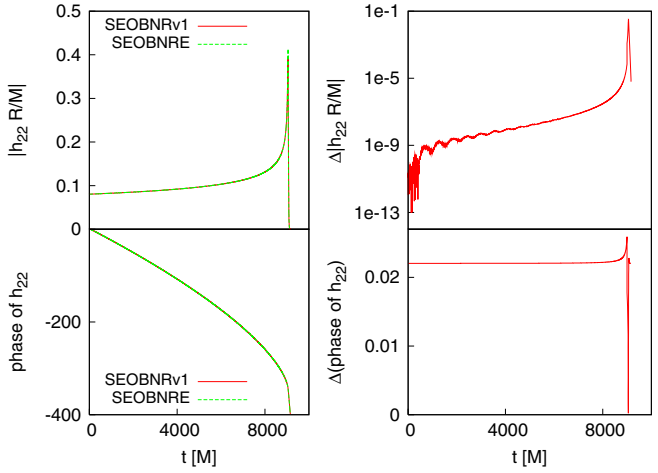

FIG. 2. Quantitative comparison of waveform h_{22} corresponding to Fig. 1. In the plot, $\Delta|h_{22}R/M| \equiv \mathrm{abs}(|h_{22,\mathrm{SEOBNRE}}R/M| - |h_{22,\mathrm{SEOBNRv1}}R/M|)$, $\Delta(\mathrm{phase\ of}\ h_{22}) \equiv \mathrm{abs}(\mathrm{phase\ of}\ h_{22,\mathrm{SEOBNRE}} - \mathrm{phase\ of}\ h_{22,\mathrm{SEOBNRv1}})$.

spinless black holes with an equal mass. In Fig. 1 $t^{22}_{\mathrm{match}} \approx 9048.1579M$. The overlap factor between the two waveforms shown in Fig. 1 is $\mathcal{O} = 0.99998$. At the same time, we have also checked the energy flux $-\frac{dE}{dt}|_{(C)}$ introduced in [34] which is shown in (C1) and the elliptical orbit correction we calculated in (63). We find that the energy flux (C1) can describe the real flux used by SEOBNRE dynamics (60) quite well in the early inspiral stage but fails at the late inspiral and plunge stage. At later times, the energy flux (C1) even becomes positive, which is unphysical. This implies that the PN energy flux expression breaks down at the late inspiral and plunge stage.

In Fig. 2, we compare the waveform h_{22} more quantitatively, where the amplitude and phase are considered. Regarding the elliptical orbit correction terms, as one expects, they are ignorable before plunge in this quasicircular case as shown in the bottom panel of Fig. 1. Near the merger, our elliptic correction terms fail to distinguish a real eccentric orbit with the plunge behavior in the quasicircular orbit, so the difference for both the amplitude and phase increase. At the merger, the differences for the amplitude and phase get maximal values, about 0.03 and 0.026 rad, respectively. As shown in Figs. 1 and 2, our SEOBNRE model can recover the SEOBNRv1 result somewhat well. In Figs. 1 and 2, we align the time at the simulation start time $(t = 0)$, which corresponds to a gravitational wave frequency $Mf_0 \approx 0.004$. For two $10\mathrm{M}_\odot$ black holes, $f_0 = 40\,\mathrm{Hz}$. At this alignment time, we also set the phase of the gravitational wave 0, which makes the comparison easier.

Our second testing case is two identical spinless black holes with an eccentricity $e_0 = 0.003$ at $Mf_0 \approx 0.001477647$, which corresponds to two $10\mathrm{M}_\odot$ black holes with $f_0 = 15$ Hz. As shown in Fig. 3, we can see clearly the oscillation of a radial coordinate r with respect to time, which corresponds to the eccentric orbital motion. But this level of eccentricity is ignorable for a waveform as shown in Fig. 4. Although small, we can see the oscillation behavior of the energy flux with the same frequency to the r motion in the bottom panel of Fig. 4. And again, we find that the energy flux (C1) can describe the real flux quite well in the early inspiral stage but fails at a late inspiral and plunge stage. In Figs. 3 and 4, we have adjusted the time coordinate of $e_0 = 0$

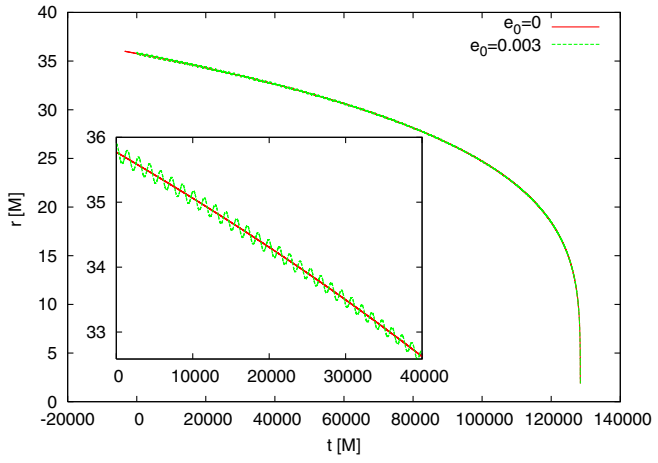

FIG. 3. Test for two identical spinless black holes with eccentricity $e_0 = 0.003$ at $Mf_0 \approx 0.0015$. The comparison of orbital evolution for $e_0 = 0.003$ and $e_0 = 0$. The result of $e_0 = 0$ is from the SEOBNRv1 code, and the $e_0 = 0.003$ result is from the SEOBNRE model. The inset of the plot is the blowup of the corresponding range.

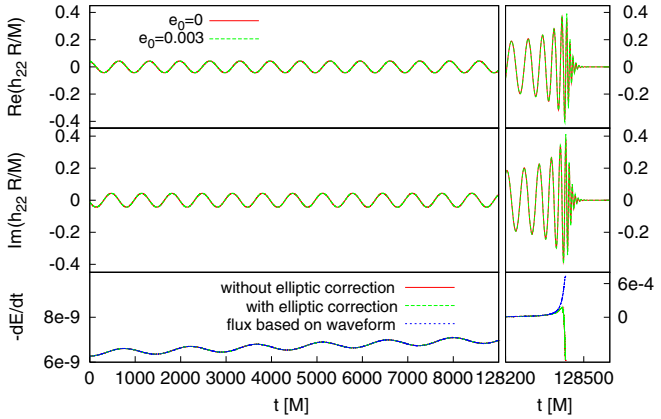

FIG. 4. Similar to Fig. 1 but for two identical spinless black holes with an eccentricity $e_0 = 0.003$ at $Mf_0 \approx 0.0015$. The result of $e_0 = 0$ is determined by the SEOBNRv1 code, and the $e_0 = 0.003$ result is from the SEOBNRE model.

result to align with the merger time of $e_0 = 0.003$, which is $t^{22}_{\rm match} \approx 128427.86M$. The overlap factor between the two waveforms shown in Fig. 4 is $\mathcal{O} = 0.99995$.

When we increase the eccentricity to $e_0 = 0.03$ for $Mf_0 \approx 0.001477647$, the radial oscillation becomes stronger than that of Fig. 3. But the overall behavior is similar. Regarding the waveform, a phase difference to a quasicircular case appears as shown in Fig. 5. More quantitatively, the amplitude difference and the phase difference are shown in Fig. 6. Along with the time, the two differences decrease. This is because the eccentricity is decreasing due to the circularizing effect of a gravitational radiation. Near a merger, such a difference almost disappears. This result supports our assumption that we ignore the effect of eccentricity on the mass and spin of the final Kerr black hole in (69) and (70). Near the merger, the difference becomes larger again. But we note that the maximal difference is 0.03 and 0.02 rad for the amplitude

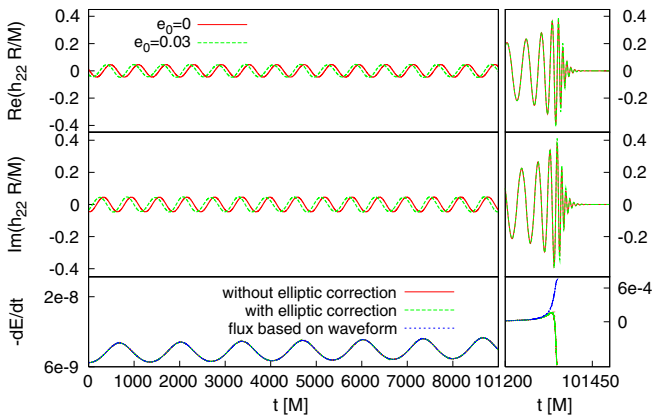

FIG. 5. Similar to Fig. 1 but for two identical spinless black holes with an eccentricity $e_0 = 0.03$ at $Mf_0 \approx 0.0015$. The result of $e_0 = 0$ is from the SEOBNRv1 code, and the $e_0 = 0.03$ result is from the SEOBNRE model.

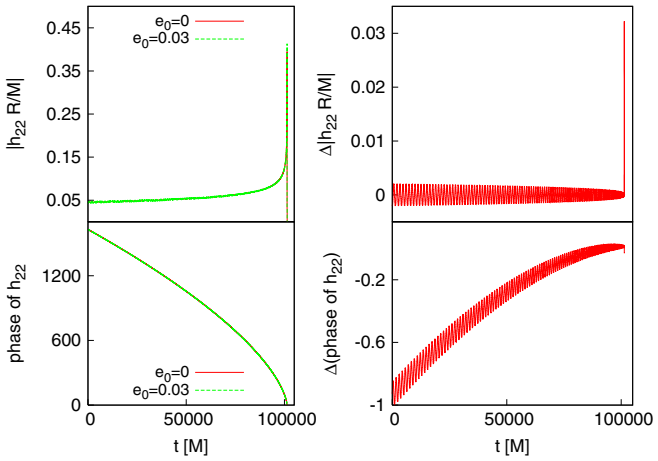

FIG. 6. Amplitude and phase comparison for h_{22} corresponding to the case $e_0 = 0.03$ shown in Fig. 5. The result of $e_0 = 0$ is from the SEOBNRv1 code, and the $e_0 = 0.03$ result is from the SEOBNRE model.

and phase, respectively. This level of difference is the same as the one we determined for the quasicircular case shown in Fig. 2. So we believe this resulted from the same reason as in quasicircular case. Similar to Fig. 4, we here have adjusted the time coordinate of $e_0 = 0$ result to align with the merger time of $e_0 = 0.03$, which is $t^{22}_{\rm match} \approx 101345.99M$. The overlap factor between the two waveforms shown in Fig. 5 is $\mathcal{O} = 0.99300$.

When we increase the eccentricity more to $e_0 = 0.3$ for $Mf_0 \approx 0.001477647$, the radial oscillation becomes much stronger as expected while the overall behavior is similar to that of Fig. 3. Regarding the waveform, the oscillation behavior of the amplitude can be clearly seen as shown in Fig. 7. The amplitude difference and the phase difference are quantitatively shown in Fig. 8. The overall behavior is similar to that of Fig. 6. In this case, the maximal difference

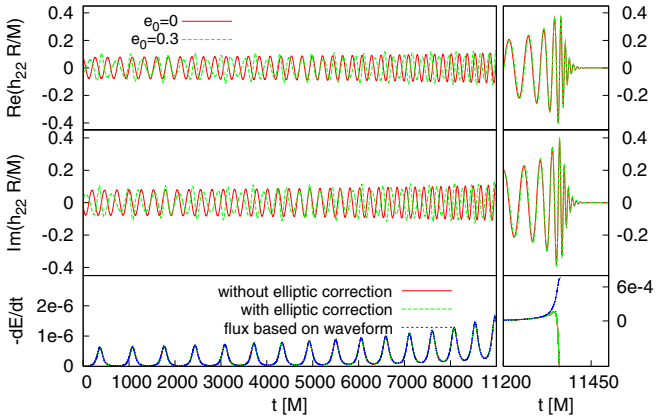

FIG. 7. Similar to Fig. 1 but for two identical spinless black holes with eccentricity $e_0 = 0.3$ at $Mf_0 \approx 0.0015$. The result of $e_0 = 0$ is from the SEOBNRv1 code, and the $e_0 = 0.3$ result is from the SEOBNRE model.

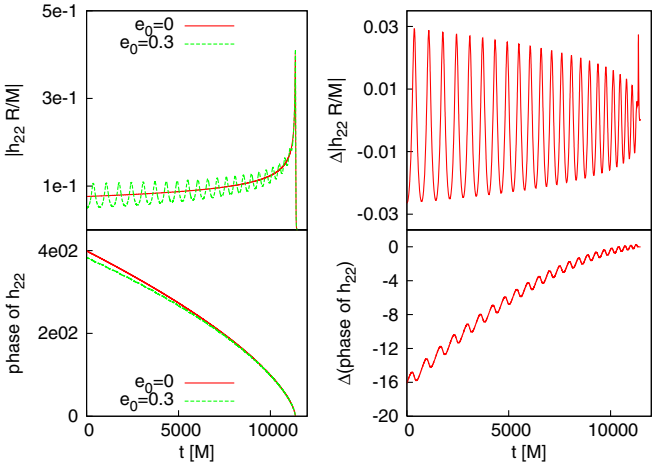

FIG. 8. Amplitude and phase comparison for h_{22} corresponding to the case shown in Fig. 7. The result of $e_0 = 0$ is from the SEOBNRv1 code, and the $e_0 = 0.3$ result is from the SEOBNRE model.

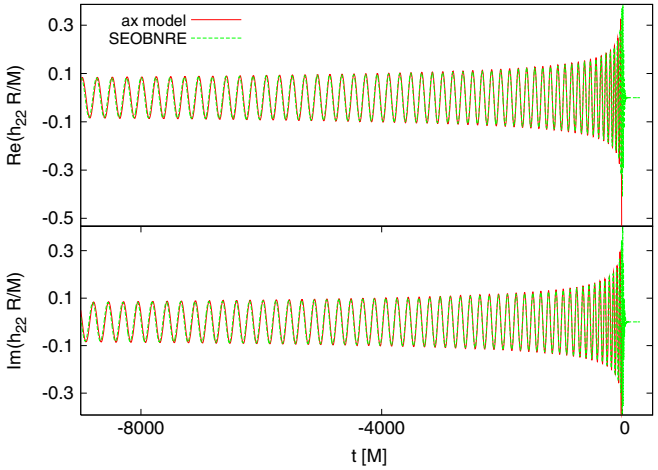

FIG. 9. Comparison between the ax model and the SEOBNRE model for the $e_0 = 0$ case.

in the early inspiral stage is 0.03 and 16 rad for the amplitude and phase, respectively. Similar to Fig. 4, we here have adjusted the time coordinate of $e_0 = 0$ result to align with the merger time of $e_0 = 0.3$ which is $t^{22}_{\rm match} \approx 11357.098M$. The overlap factor between the two waveforms shown in Fig. 7 is $\mathcal{O} = 0.46942$.

When the initial eccentricity e_0 becomes bigger than 0.6 for $Mf_0 \approx 0.001477647$, we find that the correction term of the waveform (51) becomes significant which means the perturbation assumption of the small eccentricity breaks down. This situation may be improved by a higher order post-Newtonian result for an eccentric orbit binary. But unfortunately, the higher order PN results for an eccentric orbit binary is not yet available. Of course, this does not mean our model can be applied to $e_0 < 0.6$ cases. Cases with such large eccentricity need more tests against, for example, numerical relativity simulations. The tests done in this subsection indicate that our SEOBNRE model can give consistent results compared to the quasicircular case.

B. Comparison to advanced *x* model (ax model)

In [36], the authors proposed a x model to describe the gravitational waveform for an eccentric orbital binary black hole. For the early inspiral stage, the authors of [36] showed consistency between the x model and the numerical relativity simulation result. Noting that the x model is based on a low order post-Newtonian approximation, Huerta and his coworkers improved the x model with high order PN results to get an advanced x model (ax model) in [34]. The full ax model includes inspiral, merger, and ringdown stages. Similar to our treatment about a merger and ringdown, the ax model also makes the assumption that the eccentricity is small and has been dissipated away before the merger. So here, we only compare our SEOBNRE model to an ax model for the inspiral part.

In the ax model, the adiabatic picture is taken. So the eccentricity itself is treated as a dynamical variable. In all, the ax model includes dynamical variables eccentricity e, reduced orbital frequency $x \approx (\omega M)^2/3$ with ω the orbital frequency, the mean anomaly l, and the relative angular coordinate ϕ. In the comparison here, we take the initial data $x = 0.05$, $l = \phi = 0$ and vary e.

Firstly, we compare the $e_0 = 0$ case in Fig. 9. Overall the two waveforms show very good consistency, which corresponds to the result of a fitting factor 0.95 with respect to the advanced LIGO determination in [34]. But we can still see some amplitude differences near the merger, and some phase differences when the evolution time becomes longer. Since we have confirmed our SEOBNRE model in Figs. 1 and 2 for the $e_0 = 0$ case, we attribute this difference to the relatively low order PN approximation of an ax model. Effectively, the EOBNR model admits more than a 3.5 PN order [7,72]; this is why we call the ax model a relatively low PN order. The overlap factor between the two waveforms (inspiral part, $t < 0$) shown in Fig. 9 is $\mathcal{O} = 0.99802$.

In contrast to the ax model, the eccentricity is not an explicitly dynamical variable in the SEOBNRE model. And limited by the simplified method, we have taken to treating the initial data described in the above section; we start our SEOBNRE simulation from the somewhat low frequency $Mf_0 \approx 0.001477647$ and vary different e_0 to fit the ax model result. The fitting process has not been optimized, so the real consistency result may be better than the ones presented here. We have considered two concrete examples. The first example is $e_0 = 0.1$ at $x_0 = 0.05$ for an ax model and $e_0 = 0.15$ at $Mf_0 \approx 0.001477647$ for the SEOBNRE model. The initial eccentricity for the SEOBNRE model is larger. We suspect this is because the effective initial separation implemented in the SEOBNRE model is larger than the one in an ax model. After some evolution time, the circularization effect drives the eccentricity within the SEOBNRE model to the one presented in an ax model.

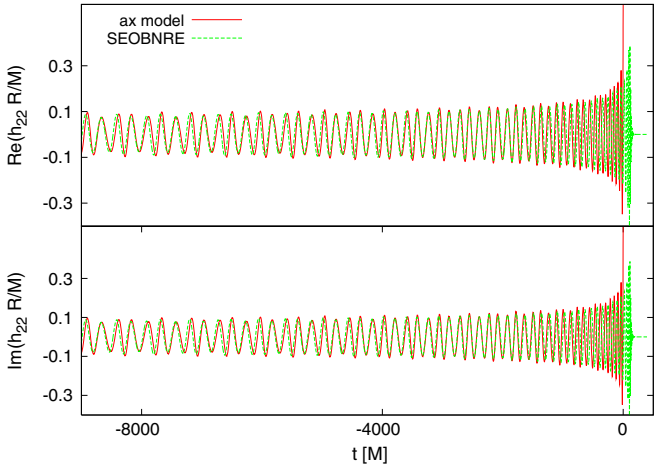

FIG. 10. Comparison between an ax model ($e_0 = 0.1$, $x_0 = 0.05$) and the SEOBNRE model ($e_0 = 0.15$, $Mf_0 \approx 0.001477647$).

The comparison result is shown in Fig. 10. We can see the consistency of the amplitude and phase between the ax model and the SEOBNRE model lasts more than 8000 M. The overlap factor between the two waveforms shown in Fig. 10 is $\mathcal{O} = 0.93031$. Our second example is the comparison between $e_0 = 0.3$ at $x_0 = 0.05$ of the ax model and $e_0 = 0.4$ at $Mf_0 \approx 0.001477647$ of the SEOBNRE model. The result is shown in Fig. 11. The consistency of the amplitude and phase between an ax model and the SEOBNRE model lasts about 5000 M. The overlap factor between the two waveforms shown in Fig. 11 is $\mathcal{O} = 0.66617$.

C. Comparison to numerical relativity results

No matter how reasonable, we have taken several approximations when we construct our SEOBNRE model. In contrast to this situation, numerical relativity solves the Einstein equation directly [73]. Up to the numerical error, the results given by numerical relativity is the exact solution to the Einstein equation. So we can use the simulation results by numerical relativity to check and calibrate the validity of the SEOBNRE model. Since the EOBNR models have been well calibrated to numerical relativity results for circular cases, and our SEOBNRE model can recover the usual EOBNR model as shown in Figs. 1 and 2 for $e_0 = 0$ case, there is no surprise that our SEOBNRE model is consistent to quasicircular simulation results of numerical relativity.

For eccentric cases, there are some subtleties in defining the eccentricity due to the "in"-spiral effect reduced by the gravitational radiation. In this work, we are not intending to touch this subtle problem involved in numerical relativity [74,75]. Instead, we take the similar recipe adopted in the above subsection to do the comparison. For a given numerical relativity simulation result, we vary the initial eccentricity e_0 corresponding to $Mf_0 \approx 0.001477647$ for SEOBNRE to fit the numerical relativity result. Again the fitting process is not optimized, so the consistency between our SEOBNRE model and the numerical relativity result may be better than the ones presented here.

We have done three comparisons in the current work. The numerical relativity simulation results come from the public data [76], which are calculated by the SPEC code [77]. The first one is the waveform SXS:BBH:0091 [76], which corresponds to an equal mass, spinless binary black hole with an initial eccentricity $e_0 = 0.02181$ starting to evolve at an orbital frequency $Mf_0 = 0.0105565727235$. On the SEOBNRE side, the initial eccentricity is $e_0 = 0.1$ starting to evolve at an orbital frequency $Mf_0 = 0.001477647$, which is the same as the ones shown in previous figures. The comparison is presented in Fig. 12.

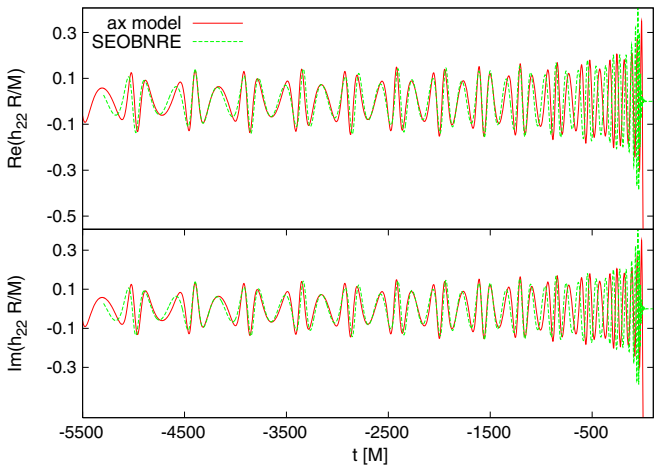

FIG. 11. Comparison between the ax model ($e_0 = 0.3$, $x_0 = 0.05$) and the SEOBNRE model ($e_0 = 0.4$, $Mf_0 \approx 0.001477647$).

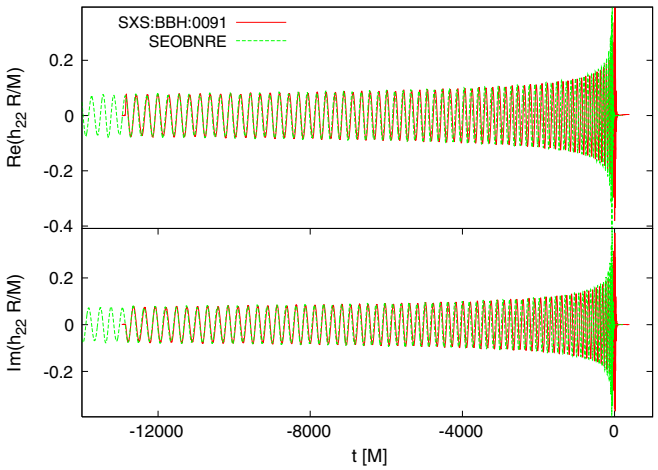

FIG. 12. SXS:BBH:0091 one is the SPEC simulation result for an equal mass spinless binary black hole with $e_0 = 0.02181$ at an orbital frequency 0.0105565727235. The SEOBNRE one corresponds to $e_0 = 0.1$ at $Mf_0 \approx 0.001477647$ for an equal mass spinless binary black hole.

Although the eccentricity involved in this comparison is somewhat small, the oscillation of the gravitational waveform amplitude is clear. The consistency for both the amplitude and the phase is quite good. The overlap factor between the two waveforms shown in Fig. 12 is $\mathcal{O} = 0.99201$. At the same time, we also note that the overlap factor between the numerical relativity waveform and the $e_0 = 0$ SEOBNRE waveform is 0.990. Our second comparison for a numerical relativity simulation result is SXS:BBH:0106 [76]. Both the numerical relativity simulations result and the SEOBNRE simulation admit exactly the same eccentricity parameters as the first comparison. The only difference to the first comparison is the mass ratio for the binary black hole, which is 5:1 here. The comparison is shown in Fig. 13. The overlap factor between the two waveforms shown in Fig. 13 is $\mathcal{O} = 0.99739$. In contrast, the overlapping factor between the numerical relativity waveform and the $e_0 = 0$ SEOBNRE waveform is 0.989. Interestingly, we find that the consistency between the numerical relativity result and the SEOBNRE result is even better than the first one. The SEOBNRE result can recover the numerical relativity result for the whole inspiral-merger-ringdown process. We can understand this result as follows. As shown by Peters through a post-Newtonian approximation in [19], the decay of an eccentricity and the lifetime for the binary can be estimated

$$\frac{de}{dt} = -\frac{304}{15}\frac{M^3\eta}{a^4(1-e^2)^{5/2}}e\left(1+\frac{121}{304}e^2\right), \quad (73)$$

$$T(a_0, e_0) = \frac{768}{425}\frac{5a_0^4}{256M^3\eta}(1-e_0^2)^{7/2}, \quad (74)$$

where a means the separation (semimajor axis) of the binary, and the subindex 0 means the initial quantities. Definitely this estimation can not be correct for the late inspiral and merger stages considered in the current paper. But this estimation can give us a qualitative picture. Compare Figs. 12 and 13, we can see the lifetime for the mass ratio 5:1 binary is much shorter than the one for the equal mass case. According to the above lifetime estimation, we can deduce that the initial separation for a mass ratio 5:1 binary is shorter than that of an equal mass one. The initial separations used in the numerical relativity simulations are 19 for an equal mass binary and 14 for a mass ratio 5:1 binary, respectively. Although these separation values are gauge dependent, they show consistency to the PN prediction. Then noting that the eccentricity decay is proportional to the fourth power of a, we can expect that the eccentricity decay involved in Fig. 13 case is much faster than that in Fig. 12. Faster eccentricity decay results in a smaller eccentricity during the later process. So our small eccentricity assumption works better.

Our third comparison investigates a larger eccentricity case for an equal mass binary. On the numerical relativity simulation side, the initial eccentricity is $e_0 = 0.1935665$ starting to evolve at an orbital frequency $Mf_0 = 0.0146842176288$. The eccentricity is about 1 order larger than the above two cases. The simulation data correspond to SXS:BBH:0323 [76]. The mass ratio of the two black holes in this simulation is 11:9. And the dimensionless spins for the big and small black hole are 0.33 and −0.44, respectively. On the SEOBNRE side, the initial eccentricity is $e_0 = 0.3$ starting to evolve at an orbital frequency $Mf_0 = 0.001477647$. The comparison is shown in Fig. 14. During the inspiral stage, we can see the waveform amplitude and phase are roughly consistent between the numerical

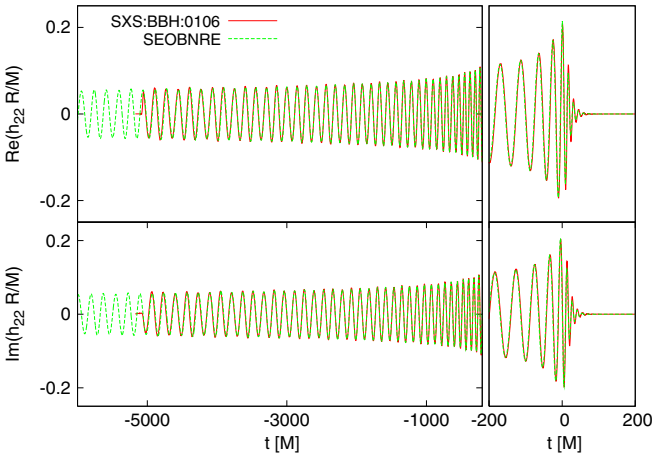

FIG. 13. SXS:BBH:0106 one is the SPEC simulation result for two spinless black holes with a mass ratio 1:5 start orbit with $e_0 = 0.02181$ at an orbital frequency 0.0105565727235. The SEOBNRE one corresponds to $e_0 = 0.1$ at $Mf_0 \approx 0.001477647$ for two spinless black holes with a mass ratio 1:5.

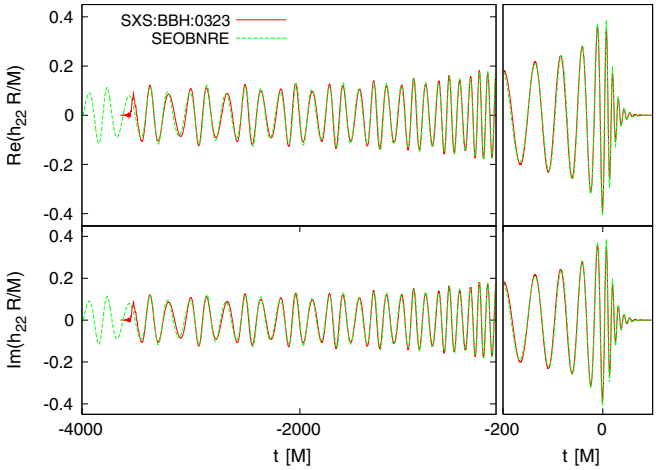

FIG. 14. SXS:BBH:0323 one is the SPEC simulation result for two spinless black holes with an equal mass start orbit with $e_0 = 0.1935665$ at an orbital frequency 0.0146842176288. SEOBNRE one corresponds to $e_0 = 0.3$ at $Mf_0 \approx 0.001477647$ for two black holes with a mass ratio 11:9 and spin $\chi_1 = 0.33$ and $\chi_2 = -0.44$, respectively, which corresponds to the setting of SXS:BBH:0323.

relativity result and the SEOBNRE result. The overlap factor between the two waveforms shown in Fig. 14 is $\mathcal{O} = 0.98171$. In contrast, the overlap factor between the numerical relativity waveform and the $e_0 = 0$ SEOBNRE waveform is 0.849. Because of the larger eccentricity, the consistency is not as good as the $e_0 \approx 0.02$ cases shown in Figs. 12 and 13. But we can note that the consistency is quite good for the merger and ringdown stage. We suspect this is because the eccentricity has decayed quite an amount, so the consistency improves during these stages.

D. Comparison to Teukolsky equation results for an extreme mass ratio binary

The largest mass ratio of binary black holes investigated by numerical relativity is 100∶1 [15]. But the simulation only lasts two orbits, which is too short to be used for a gravitational waveform analysis. Until now, the mass ratio of a binary black hole investigated by numerical relativity for gravitational waveform usage is less than 20∶1 [9–12]. This limitation of numerical relativity is due to the computational cost for a finite difference code, and/or due to the complicated computational grid adjustment for a spectral code. In the future, the finite element code may be some help for this problem [78–80]. But it is still under development. In contrast, our SEOBNRE model is free from this kind of limitation. This is similar to all other EOBNR models.

When the mass ratio becomes quite large, the small black hole can be looked as a perturbation source with respect to the spacetime of the large black hole. Consequently, the Teukolsky formalism is reasonable to treat this kind of binary problem. In [39], we constructed such a model to investigate the extreme mass ratio binary system. In [38], one of us applied such a model to investigate the eccentric binary black holes. It is interesting to compare the results found in [38] and the ones simulated with the SEOBNRE model proposed here.

In all we have tested four cases. All of them are binary black holes with a mass ratio about 1000∶1. More accurately, the symmetric mass ratio is $\eta = 10^{-3}$. The dynamical variables involved in the Teukolsky model [38,39] are the same as the ones in the SEOBNRE model. So for the comparison in this subsection, we set the initial data for the SEOBNRE model exactly the same as the ones for the Teukolsky model. More concretely, within spherical coordinate, we set $r_0 = \frac{p_0}{1+e_0}$ with $p_0 = 12$, $e_0 = 0.3$, $\phi_0 = 0$, $p_{r_0} = 0$, and p_{ϕ_0}, similar to the Fig. 4 of [38].

Not like the above test cases, which involve slowly spinning black holes considered in previous subsections, the four test cases here admit high-spin black holes. We set the big black hole spinning while leaving the small black hole spinless. The spin parameters χ for the four test cases are 0.9, 0.5, −0.5, and −0.9, respectively. Here, the negative value means the spin direction is antiparalleled to the direction of the orbital angular momentum of the binary. And the parameters p_{ϕ_0} for the initial data are 3.75295952324398, 3.86330280736881, 4.19862434393390, and 4.35790829850906, respectively. Different to the Fig. 4 of [38], here we have fixed $p_0 = 12$ while varied p_{ϕ_0} for corresponding χ. This setting makes it easier to check the effect of χ on the gravitational waveform.

The gravitational waveform description adopted in [38] used $h_{+,\times}$ (note the y-axis label typos involved in the Fig. 4 of [38]). In order to make the comparison easier between the results in current paper and the ones in [38], we also adopt $h_{+,\times}$ to describe the gravitational waveform in this subsection. This is different to the spherical harmonic modes description used in previous subsections. Here, we ignore the higher than 22 spherical harmonic modes and relate the $h_{+,\times}$ to h_{22} through

$$h_+ - ih_\times = h_{22}{}^{-2}Y_{22} + h_{22}^*{}^{-2}Y_{2-2}, \tag{75}$$

where we have used the relation $h_{2-2} = h_{22}^*$ with an upper star denoting the complex conjugate [58]. Then, $h_{+,\times}$ are functions of direction angles. Following the Fig. 4 of [38], we plot $h_{+,\times}(\frac{\pi}{2}, 0)$ in Fig. 15. Overall, we can see that the consistency between the results of the Teukolsky model and the ones of the SEOBNRE model is good. When the comparison time becomes longer, the phase difference shows up. In Fig. 16, we compare the phase of $h_+ - ih_\times$ corresponding to the cases shown in Fig. 15.

As mentioned above, the four cases admit the same initial separation parameter $p_0 = 12$. Based on Newtonian gravity, the same mass ratio, the same initial separation, and

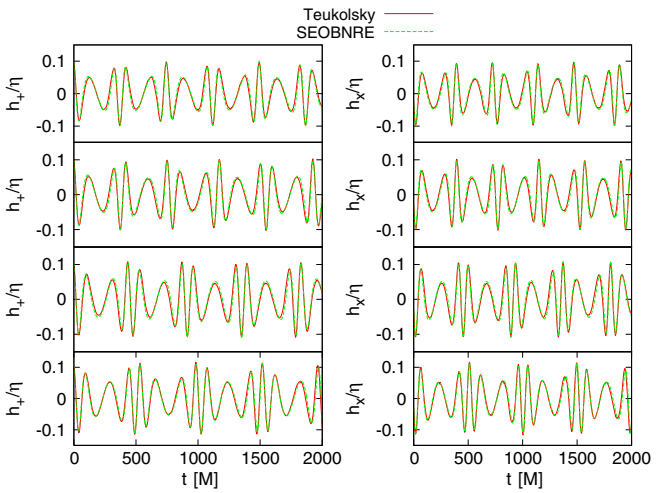

FIG. 15. Comparison between the Teukolsky equation based model (marked with 'Teukolsky') and the SEOBNRE model. All cases here admit a mass ratio about 1∶1000, initial eccentricity $e_0 = 0.3$, and the initial separation parameter $p_0 = 12$. From top row to bottom row, the corresponding initial orbital angular momentum are $\chi = 0.9$, $p_{\phi_0} = 3.75$; $\chi = 0.5$, $p_{\phi_0} = 3.86$; $\chi = -0.5$, $p_{\phi_0} = 4.20$, and $\chi = -0.9$, $p_{\phi_0} = 4.36$, respectively.

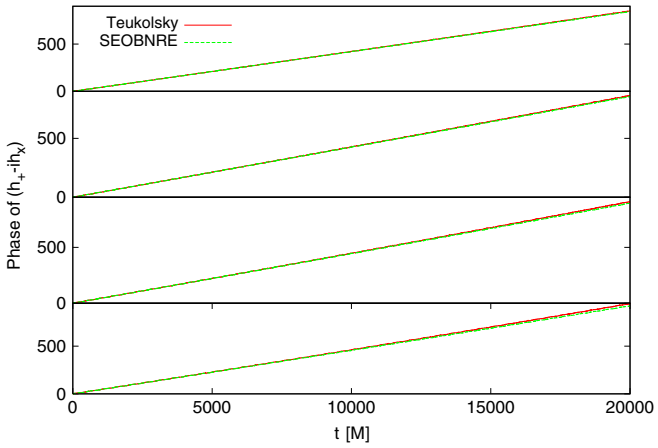

FIG. 16. Phase comparison of $h_+ - ih_\times$ between the Teukolsky equation based model and the SEOBNRE model. Cases correspond to those of Fig. 15, respectively.

the same eccentric setting may roughly reduce the same orbital angular frequency. But we can see the larger χ ones admit a little bit faster frequency of a gravitational waveform, while correspondingly, a smaller orbital angular momentum p_{ϕ_0} ($3.75 < 3.86 < 4.20 < 4.36$). We attribute this to the faster frame dragging effect of the big black hole. In order to stay at the same radius position, corotating objects need a smaller orbital angular momentum, but the antirotating objects need a larger orbital angular momentum. And the frame dragging effect makes the gravitational wave frequency bigger for the corotating case while smaller for the antirotating case.

The overlap factors between the two respective waveforms for the cases shown in Fig. 15 are $\mathcal{O} = 0.985367$, 0.985209, 0.986240, and 0.985558 for $\chi = 0.9$, 0.5, −0.5, and −0.9, respectively. When the comparison time increases to 20000 M, the overlap factors decrease to 0.690179, 0.672447, 0.549308, and 0.498645, respectively. One caution is in order here. Neither the SEOBNRE model nor the Teukolsky model is guaranteed to be accurate at 1 post-adiabatic order. So the good overlapping does not mean either model is accurate enough for gravitational wave detection usage. Since the two models make different approximations and therefore introduce different errors, the good overlapping does imply those differences are ignorable for the compared cases. Only when one post-adiabatic results are available, our SEOBNRE model can be checked more quantitatively for extreme mass ratio systems.

IV. DISCUSSION AND CONCLUSION

The EOBNR model has contributed much to the gravitational wave detection. But the existing EOBNR models are limited to quasicircular ($e = 0$) systems. Without a doubt, the EOBNR model will continue to play an important role in the following LIGO observations. After about 20 years, space-based detectors will begin to work. It is interesting and important to ask whether the EOBNR model can still play an important role in the space-based gravitational wave detection. Among the gravitational wave sources for space-based detectors, binary systems are important. And many such binary systems admit an eccentric orbital motion [81]. A partial reason for this fact is that the decay rate of the eccentricity is proportional to the symmetric mass ratio. So although it may be not all of the issues limiting the EOBNR model to work for space-based detectors, the eccentric orbit problem is an important point blocking the EOBNR model to work for space-based detectors. So it is quite important to extend the EOBNR model to describe eccentric binary systems. We proposed the first such extending model in the current paper—the SEOBNRE model.

Our idea for constructing the SEOBNRE model is combining the existing excellent property of EOBNR models for quasicircular binary and the corrections coming from the eccentric orbit motion. The strategy is expanding, involving quantities with respect to the eccentricity by assuming the smallness of the eccentricity. Then we calculate the correction terms coming from the eccentricity through the post-Newtonian approximation. Although the post-Newtonian order of the correction terms we determine is only to second order, we expect that such kinds of correction terms may work well. The reason is because when the eccentricity is large, the separation of the binary is also large, then a relative low order post-Newtonian approximation is necessary. Along with the decreasing of the separation of the binary, the eccentricity also decreases due to the circularizing effect of the gravitational radiation. Consequently, the correction terms contribution is weaker and weaker. In contrast, although the high PN order approximation is needed due to the decrease of the separation, the existing excellent property of the EOBNR model can do the job.

Our SEOBNRE model includes a Hamiltonian [Eq. (17)], waveform expression [Eqs. (52) and (68)] and the related energy flux [Eq. (60)]. We have compared our SEOBNRE model against the quasicircular EOBNR model for a consistency check. For $e = 0$, the SEOBNRE model can recover the existing EOBNR models well. When the eccentricity e increases, the difference between the SEOBNRE model and the quasicircular EOBNR model grows. We have introduced an overlap factor as defined in (71) to quantify this difference. When $e < 0.03$, the difference is small. The corresponding overlap factor is larger than 0.99. When $e > 0.1$, the overlap factor becomes very low. As an example, the overlap factor for $e = 0.3$ becomes 0.47. This result added evidences to the literature [33] that a quasicircular template will break down when the eccentricity becomes larger than 0.1.

We have also compared the SEOBNRE model against another eccentric binary waveform model—the ax model [34]. When $e < 0.15$, the overlap factor between the ax model and the SEOBNRE model is bigger than 0.9. This implies the consistency between the ax model and the SEOBNE model. As an example of the $e > 0.2$ cases, the

overlap factor for $e = 0.3$ between the ax model and the SEOBNRE model is as low as 0.67. This cautions us that more investigations are needed for the waveform model about highly eccentric binary.

Numerical relativity (NR) simulation results can be looked as the standard answer for the eccentric binary. We have tested three numerical relativity simulation results. These three cases include spinless binary and spinning binary, equal mass binary, and unequal mass binary. Compared to NR simulations with eccentricity 0.02, 0.02, and 0.19, the overlap factor for SEOBNRE model is 0.992, 0.997, and 0.982, respectively. In contrast, the overlap factor between a NR waveform and a $e = 0$ SEOBNRE waveform is 0.990, 0.989, and 0.849, respectively.

Motivated by the gravitational wave sources for a space-based detector, we have applied the SEOBNRE model to extreme mass ratio binaries. Specifically, we considered binaries with a mass ratio 1 to 1000. Since numerical relativity is not available yet for this kind of binaries, we compared the SEOBNRE model against the Teukolsky equation based model. Both spin aligned cases and anti-aligned cases are considered. All cases admit a high eccentricity $e = 0.3$. If we only care about time lasting several thousands M, the overlap factor between the SEOBNRE model and the Teukolsky equation based model is then 0.9. For a total mass $M = 10^6$, solar mass binaries of several thousands M corresponds to the time of hours. If we consider avlasting time with tens of thousands M, the overlap factor drops below 0.7. Although the Teukolsky equation based model does not represent the standard answer as numerical relativity, this result also reminds us more work is needed when a long duration time is involved.

In the current paper, a simple overlap factor is considered to quantify the accuracy of the SEOBNRE model. For realistic gravitational wave detection, a much more detailed accuracy requirement [82–86] is needed. It is interesting to ask if our SEOBNRE model is ready or not for particular detection projects, such as eLISA [24], LISA [26], Taiji [27], and Tianqin [28]. We leave such investigation as future works. On the other hand, there at least two possible clues to improve the SEOBNRE model. The first one is calculating higher PN order terms for the eccentric correction. The second one is the trick adopted by Pan and his coworkers when they developed the EOBNR model [7]. The trick is adding some tuning parameters into the SEOBNRE model and then requiring these parameters to fit the calibration waveform such as numerical relativity simulation results. Noting that we did not put in any tunable parameters in the eccentric correction terms, there are two strategies to apply the mentioned trick. The first one is adjusting the existing parameters introduced in the original EOBNR models. The second one is adding more parameters into the eccentric correction terms and adjusting them.

Regarding the merger and ringdown parts waveform (68), the possible improvement is taking the effect of the eccentricity on the mass and the spin of the final Kerr black hole into consideration. This point needs many more numerical relativity simulations to extend the relations (69) and (70) to include eccentricity. We leave these investigations to future study.

ACKNOWLEDGMENTS

This work was supported by the NSFC (Grants No. 11690023, No. 11622546, No. 11375260, and No. U1431120). Z. C. was also supported by "the Fundamental Research Funds for the Central Universities". W. H. was also supported by Youth Innovation Promotion Association CAS and QYZDB-SSW-SYS016 of CAS.

APPENDIX A: DETAIL EXPRESSIONS FOR THE SEOBNRE HAMILTOANIAN

The SEOBNR Hamiltonian develops gradually, so the overall expressions are spread throughout the literature. In this Appendix section, we collect all the results for the SEOBNR Hamiltonian together. Our major references are [51,56]. The involved terms corresponding to Eq. (18) can be expressed as the following:

$$\frac{H_{NS}}{M\eta} = \beta^i p_i + \alpha\sqrt{1 + \gamma^{ij} p_i p_j + Q_4(p)}, \tag{A1}$$

$$\begin{aligned}\frac{H_S}{M\eta} &= \omega S_{\hat{a}} + \omega_r \frac{e^{-3\mu-\nu}\sqrt{\Delta_r}}{2B(1+\sqrt{Q})\sqrt{Q}\xi^2}[e^{2(\mu+\nu)} p_\xi^2 S_v r^2 - B e^{\mu+\nu} p_v p_\xi S_\xi r^2 + B^2\xi^2(e^{2\mu}(\sqrt{Q}+Q)S_v + p_n p_v r S_n\sqrt{\Delta_r} - p_n^2 S_v \Delta_r)] \\ &+ \omega_{\cos\theta}\frac{e^{-3\mu-\nu}\sqrt{\Delta_r}}{2B(1+\sqrt{Q})\sqrt{Q}}[S_n(-e^{2(\mu+\nu)} p_\xi^2 r^2 + B^2(p_v^2 r^2 - e^{2\mu}(\sqrt{Q}+Q)\xi^2)) - B p_n(B p_v S_v - e^{\mu+\nu} p_\xi S_\xi) r\sqrt{\Delta_r}] \\ &+ \frac{e^{-\mu+2\nu}}{B^2\sqrt{Q}\xi^2}(-B + e^{\mu+\nu}) p_\xi S_{\hat{a}} r + \frac{e^{-2\mu+\nu}}{B^2(\sqrt{Q}+Q)\xi^2}\{-B e^{\mu+\nu}\nu_{\cos\theta} p_\xi r(1+2\sqrt{Q})S_n\xi^2 \\ &+ \sqrt{\Delta_r}[B(e^{\mu+\nu}\nu_r p_\xi r(1+2\sqrt{Q})S_v + B\mu_r p_v r S_\xi + B S_\xi(-\mu_{\cos\theta} p_n\xi^2 + \sqrt{Q}(\mu_r p_v r - \nu_r p_v r + (\nu_{\cos\theta} - \mu_{\cos\theta}) p_n\xi^2))) \\ &- B_r e^{\mu+\nu} p_\xi r(1+\sqrt{Q})S_v]\},\end{aligned} \tag{A2}$$

$$H_{SC} = -\frac{\eta}{2r^3}(S_*^2 - 3S_n^2) + dh_{\mathrm{eff}SS}\frac{(M\eta)^2}{r^4}aS_{\hat{a}}, \quad \text{(A3)}$$

$$\alpha = \frac{1}{\sqrt{-g^{tt}}}, \qquad \beta^i = \frac{g^{ti}}{g^{tt}},$$
$$\gamma^{ij} = g^{ij} - \frac{g^{ti}g^{tj}}{g^{tt}}, \qquad i,j = (r,\theta,\phi) \quad \text{(A4)}$$

$$Q_4(p) = 2\eta(4-3\eta)\frac{\tilde{p}_n^4}{r^2},$$
$$Q = 1 + \frac{p_v^2 r^2}{\Sigma\xi^2} + \frac{\Delta_t\Sigma}{\Lambda_t}\frac{p_\xi^2 r^2}{B^2\xi^2} + p_n^2\frac{\Delta_r}{\Sigma}, \quad \text{(A5)}$$

$$S_* = \sigma^* + \Delta_{\sigma_*}^{(1)} + \Delta_{\sigma_*}^{(2)} + \Delta_{\sigma_*}^{(3)}, \quad \sigma^* = a_1 m_2 + a_2 m_1, \quad \text{(A6)}$$

$$\Delta_{\sigma_*}^{(1)} = \frac{\eta}{12r}\{\sigma[3(Q-1)r - 8 - 36\bar{p}_n^2 r] + \sigma^*[4(Q-1)r + 14 - 30\bar{p}_n^2 r]\}, \quad \text{(A7)}$$

$$\Delta_{\sigma_*}^{(2)} = \frac{\sigma}{144r^2}\{4(51\eta^2 - 109\eta)(Q-1)r - 16[7\eta(8+3\eta)] + 810\eta^2\bar{p}_n^4 r^2 - 45\eta(Q-1)^2 r^2 - 6\bar{p}_n^2 r(16\eta + 147\eta^2 + (39\eta^2 - 6\eta)(Q-1)r)\} - \frac{\sigma^*}{72r^2}\{2\eta(27\eta - 353) + 2(103\eta - 60\eta^2)(Q-1)r - 360\eta^2\bar{p}_n^4 r^2 + (23+3\eta)\eta(Q-1)^2 r^2 + 6\bar{p}_n^2 r[54\eta^2 - 47\eta + (21\eta^2 - 16\eta)(Q-1)r]\}, \quad \text{(A8)}$$

$$\Delta_{\sigma_*}^{(3)} = \frac{d_{SO}\eta}{r^3}\sigma^*, \quad \text{(A9)}$$

where S_* is the spin of the test particle deduced in the effective-one-body reduction. Following SEOBNRv1, we set $d_{SO} = -69.5$, $dh_{\mathrm{eff}SS} = 2.75$. Our setting exactly follows the SEOBNRv1 code [63]. In the above equations, we have used notations

$$\vec{n} \equiv \frac{\vec{r}}{r}, \qquad \vec{\xi} \equiv \frac{\vec{\sigma}}{\sigma} \times \vec{n}, \qquad \vec{v} \equiv \vec{n} \times \vec{\xi}, \quad \text{(A10)}$$

$$p_n \equiv \vec{p}\cdot\vec{n}, \qquad p_\xi \equiv \vec{p}\cdot\vec{\xi}, \qquad p_v \equiv \vec{p}\cdot\vec{v}, \quad \text{(A11)}$$

$$S_n \equiv \vec{S}_*\cdot\vec{n}, \qquad S_\xi \equiv \vec{S}_*\cdot\vec{\xi}, \qquad S_v \equiv \vec{S}_*\cdot\vec{v}, \quad \text{(A12)}$$

$$S_{\hat{a}} \equiv \vec{S}_*\cdot\frac{\vec{a}}{a}, \qquad \bar{p}_n \equiv \sqrt{g^{rr}}p_n, \qquad \tilde{p}_n \equiv \vec{n}\cdot\vec{\tilde{p}} \quad \text{(A13)}$$

$$\nu = \frac{1}{2}\log\left(\frac{\Delta_t\Sigma}{\Lambda_t}\right), \qquad \mu = \frac{1}{2}\log(\Sigma), \quad \text{(A14)}$$

$$\omega \equiv \frac{\tilde{\omega}_{fd}}{\Lambda_t}, \qquad B \equiv \sqrt{\Delta_t}, \quad \text{(A15)}$$

$$\nu_r \equiv \frac{r}{\Sigma} + \frac{\bar{\omega}^2(\bar{\omega}^2\Delta_t' - 4r\Delta_t)}{2\Lambda_t\Delta_t}, \qquad \mu_r \equiv \frac{r}{\Sigma} - \frac{1}{\sqrt{\Delta_r}}, \quad \text{(A16)}$$

$$\omega_r \equiv \frac{\tilde{\omega}_{fd}{}'\Lambda_t - \tilde{\omega}_{fd}\Lambda_t'}{\Lambda_t^2}, \qquad B_r \equiv \frac{\sqrt{\Delta_r}\Delta_t' - 2\Delta_t}{2\sqrt{\Delta_t\Delta_r}}, \quad \text{(A17)}$$

$$\nu_{\cos\theta} \equiv \frac{a^2\bar{\omega}^2\cos\theta(\bar{\omega}^2 - \Delta_t)}{\Lambda_t\Sigma}, \qquad \mu_{\cos\theta} \equiv \frac{a^2\cos\theta}{\Sigma}, \quad \text{(A18)}$$

$$\omega_{\cos\theta} \equiv -\frac{2a^2\cos\theta\Delta_t\tilde{\omega}_{fd}}{\Lambda_t^2}, \quad \text{(A19)}$$

where the prime denotes the derivatives with respect to r. $(\vec{r}, \vec{\tilde{p}})$ are the canonical variable within Boyer-Lindquist coordinate of the geodesic motion, while $\vec{p}$ is the momentum vector within the tortoise coordinate. $\vec{p}$ and $\vec{\tilde{p}}$ are related through [87]

$$\vec{p} = \vec{\tilde{p}} - \vec{n}(\vec{n}\cdot\vec{\tilde{p}})\frac{\xi_a - 1}{\xi_a}, \quad \text{(A20)}$$

$$\xi_a \equiv \frac{\sqrt{\Delta_t\Delta_r}}{r^2 + a^2}. \quad \text{(A21)}$$

Within a spherical coordinate $\vec{r} = (r,\theta,\phi)$, we set $\vec{a}$ along the $\theta = 0$ direction, so $\xi = \sin\theta$ in (A10).

APPENDIX B: DETAIL EXPRESSIONS FOR THE ECCENTRIC PART OF SEOBNRE WAVEFORM

In this Appendix section, we show the detailed calculation for the eccentric part of the SEOBNRE waveform. We begin with the notations introduced in Eq. (50) as the following:

$$\Theta_{ij} = \int (\epsilon_{ij}^+ - i\epsilon_{ij}^\times)^{-2}Y_{22}^* d\Omega, \quad \text{(B1)}$$

$$P_n\Theta_{ij} = \int N_n(\epsilon_{ij}^+ - i\epsilon_{ij}^\times)^{-2}Y_{22}^* d\Omega, \quad \text{(B2)}$$

$$P_v\Theta_{ij} = \int N_v(\epsilon_{ij}^+ - i\epsilon_{ij}^\times)^{-2}Y_{22}^* d\Omega, \quad \text{(B3)}$$

$$P_{nn}\Theta_{ij} = \int N_n^2(\epsilon_{ij}^+ - i\epsilon_{ij}^\times)^{-2}Y_{22}^* d\Omega, \quad \text{(B4)}$$

$$P_{nv}\Theta_{ij} = \int N_n N_v(\epsilon_{ij}^+ - i\epsilon_{ij}^\times)^{-2}Y_{22}^* d\Omega, \quad \text{(B5)}$$

$$P_{vv}\Theta_{ij} = \int N_v^2(\epsilon_{ij}^+ - i\epsilon_{ij}^\times)^{-2}Y_{22}^* d\Omega, \quad \text{(B6)}$$

$$P_{nnn}\Theta_{ij} = \int N_n^3(\epsilon_{ij}^+ - i\epsilon_{ij}^\times)^{-2}Y_{22}^* d\Omega, \quad \text{(B7)}$$

$$P_{nnv}\Theta_{ij} = \int N_n^2 N_v(\epsilon_{ij}^+ - i\epsilon_{ij}^\times)^{-2}Y_{22}^* d\Omega, \quad \text{(B8)}$$

$$P_{nvv}\Theta_{ij} = \int N_n N_v^2 (\epsilon_{ij}^+ - i\epsilon_{ij}^\times)^{-2} Y_{22}^* d\Omega, \tag{B9}$$

$$P_{vvv}\Theta_{ij} = \int N_v^3 (\epsilon_{ij}^+ - i\epsilon_{ij}^\times)^{-2} Y_{22}^* d\Omega. \tag{B10}$$

Based on Eqs. (35)–(49), direct calculation gives

$$\Theta_{ij} = \left(\frac{1}{3}\sqrt{\frac{\pi}{5}}, -\frac{i}{3}\sqrt{\frac{\pi}{5}}, 0, -\frac{1}{3}\sqrt{\frac{\pi}{5}}, \frac{8}{3\sqrt{5\pi}}, 0\right), \tag{B11}$$

$$P_n\Theta_{ij} = \left(0, 0, -\frac{\sqrt{\frac{\pi}{5}}(x_1 - ix_2)}{3\sqrt{x_1^2+x_2^2+x_3^2}}, 0, \frac{\sqrt{\frac{\pi}{5}}(ix_1 + x_2)}{3\sqrt{x_1^2+x_2^2+x_3^2}}, 0\right), \tag{B12}$$

$$P_v\Theta_{ij} = \left(0, 0, -\frac{1}{3}\sqrt{\frac{\pi}{5}}(v_1 - iv_2), 0, \frac{1}{3}\sqrt{\frac{\pi}{5}}(iv_1 + v_2), 0\right), \tag{B13}$$

$$P_{nn}\Theta_{ij} = \left(\frac{\sqrt{\frac{\pi}{5}}(-x_1^2 + 8ix_1x_2 + 7x_2^2 + x_3^2)}{21(x_1^2+x_2^2+x_3^2)}, -\frac{i\sqrt{\frac{\pi}{5}}(3x_1^2 + 3x_2^2 + x_3^2)}{21(x_1^2+x_2^2+x_3^2)}, \frac{2\sqrt{\frac{\pi}{5}}(x_1 - ix_2)x_3}{21(x_1^2+x_2^2+x_3^2)}, \right.$$
$$\left. \frac{\sqrt{\frac{\pi}{5}}(-7x_1^2 + 8ix_1x_2 + x_2^2 - x_3^2)}{21(x_1^2+x_2^2+x_3^2)}, -\frac{2i\sqrt{\frac{\pi}{5}}(x_1 - ix_2)x_3}{21(x_1^2+x_2^2+x_3^2)}, \frac{8\sqrt{\frac{\pi}{5}}(x_1 - ix_2)^2}{21(x_1^2+x_2^2+x_3^2)}\right), \tag{B14}$$

$$P_{nv}\Theta_{ij} = \left(\frac{\sqrt{\frac{\pi}{5}}(-v_1x_1 + 4iv_2x_1 + 4iv_1x_2 + 7v_2x_2 + v_3x_3)}{21\sqrt{x_1^2+x_2^2+x_3^2}}, -\frac{i\sqrt{\frac{\pi}{5}}(3v_1x_1 + 3v_2x_2 + v_3x_3)}{21\sqrt{x_1^2+x_2^2+x_3^2}}, \right.$$
$$\frac{\sqrt{\frac{\pi}{5}}(v_3(x_1 - ix_2) + (v_1 - iv_2)x_3)}{21\sqrt{x_1^2+x_2^2+x_3^2}}, \frac{\sqrt{\frac{\pi}{5}}(-7v_1x_1 + 4iv_2x_1 + 4iv_1x_2 + v_2x_2 - v_3x_3)}{21\sqrt{x_1^2+x_2^2+x_3^2}}, $$
$$\left. -\frac{\sqrt{\frac{\pi}{5}}(v_3(ix_1 + x_2) + (iv_1 + v_2)x_3)}{21\sqrt{x_1^2+x_2^2+x_3^2}}, \frac{8\sqrt{\frac{\pi}{5}}(v_1 - iv_2)(x_1 - ix_2)}{21\sqrt{x_1^2+x_2^2+x_3^2}}\right), \tag{B15}$$

$$P_{vv}\Theta_{ij} = \left(\frac{1}{21}\sqrt{\frac{\pi}{5}}(-v_1^2 + 8iv_1v_2 + 7v_2^2 + v_3^2), -\frac{1}{21}i\sqrt{\frac{\pi}{5}}(3v_1^2 + 3v_2^2 + v_3^2), \right.$$
$$\frac{2}{21}\sqrt{\frac{\pi}{5}}(v_1 - iv_2)v_3, \frac{1}{21}\sqrt{\frac{\pi}{5}}(-7v_1^2 + 8iv_1v_2 + v_2^2 - v_3^2), $$
$$\left. -\frac{2}{21}i\sqrt{\frac{\pi}{5}}(v_1 - iv_2)v_3, \frac{8}{21}\sqrt{\frac{\pi}{5}}(v_1 - iv_2)^2\right), \tag{B16}$$

$$P_{nnn}\Theta_{ij} = \left(\frac{\sqrt{\frac{\pi}{5}}(x_1 - ix_2)^2x_3}{7(x_1^2+x_2^2+x_3^2)^{3/2}}, 0, -\frac{\sqrt{\frac{\pi}{5}}(x_1 - ix_2)(2x_1^2 + 5ix_1x_2 + 7x_2^2 + 3x_3^2)}{21(x_1^2+x_2^2+x_3^2)^{3/2}}, \frac{\sqrt{\frac{\pi}{5}}(x_1 - ix_2)^2x_3}{7(x_1^2+x_2^2+x_3^2)^{3/2}}, \right.$$
$$\left. \frac{\sqrt{\frac{\pi}{5}}(ix_1 + x_2)(7x_1^2 - 5ix_1x_2 + 2x_2^2 + 3x_3^2)}{21(x_1^2+x_2^2+x_3^2)^{3/2}}, -\frac{2\sqrt{\frac{\pi}{5}}(x_1 - ix_2)^2x_3}{7(x_1^2+x_2^2+x_3^2)^{3/2}}\right), \tag{B17}$$

$$P_{nnv}\Theta_{ij} = \left(\frac{\sqrt{\frac{\pi}{5}}(x_1 - ix_2)(v_3(x_1 - ix_2) + 2(v_1 - iv_2)x_3)}{21(x_1^2+x_2^2+x_3^2)}, 0, \right.$$
$$-\frac{\sqrt{\frac{\pi}{5}}((x_1 - ix_2)(2v_1x_1 + iv_2x_1 + 4iv_1x_2 + 7v_2x_2) + 2v_3(x_1 - ix_2)x_3 + (v_1 - iv_2)x_3^2)}{21(x_1^2+x_2^2+x_3^2)}, $$
$$\frac{\sqrt{\frac{\pi}{5}}(x_1 - ix_2)(v_3(x_1 - ix_2) + 2(v_1 - iv_2)x_3)}{21(x_1^2+x_2^2+x_3^2)}, $$
$$\frac{\sqrt{\frac{\pi}{5}}((x_1 - ix_2)(7iv_1x_1 + 4v_2x_1 + v_1x_2 + 2iv_2x_2) + 2v_3(ix_1 + x_2)x_3 + (iv_1 + v_2)x_3^2)}{21(x_1^2+x_2^2+x_3^2)}, $$
$$\left. -\frac{2\sqrt{\frac{\pi}{5}}(x_1 - ix_2)(v_3(x_1 - ix_2) + 2(v_1 - iv_2)x_3)}{21(x_1^2+x_2^2+x_3^2)}\right), \tag{B18}$$

$$P_{nvv}\Theta_{ij} = \Bigg(\frac{\sqrt{\frac{\pi}{5}}(v_1 - iv_2)(2v_3(x_1 - ix_2) + (v_1 - iv_2)x_3)}{21\sqrt{x_1^2 + x_2^2 + x_3^2}}, 0,$$
$$-\frac{\sqrt{\frac{\pi}{5}}(v_3^2(x_1 - ix_2) + v_1^2(2x_1 + ix_2) + v_2^2(4x_1 - 7ix_2) - 2iv_2v_3x_3 + 2v_1(iv_2x_1 + 4v_2x_2 + v_3x_3))}{21\sqrt{x_1^2 + x_2^2 + x_3^2}},$$
$$\frac{\sqrt{\frac{\pi}{5}}(v_1 - iv_2)(2v_3(x_1 - ix_2) + (v_1 - iv_2)x_3)}{21\sqrt{x_1^2 + x_2^2 + x_3^2}},$$
$$\frac{\sqrt{\frac{\pi}{5}}(v_3^2(ix_1 + x_2) + v_2^2(-ix_1 + 2x_2) + v_1^2(7ix_1 + 4x_2) + 2v_2v_3x_3 + v_1(8v_2x_1 - 2iv_2x_2 + 2iv_3x_3))}{21\sqrt{x_1^2 + x_2^2 + x_3^2}},$$
$$-\frac{2\sqrt{\frac{\pi}{5}}(v_1 - iv_2)(2v_3(x_1 - ix_2) + (v_1 - iv_2)x_3)}{21\sqrt{x_1^2 + x_2^2 + x_3^2}}\Bigg), \tag{B19}$$

$$P_{vvv}\Theta_{ij} = \left(\frac{1}{7}\sqrt{\frac{\pi}{5}}(v_1 - iv_2)^2v_3, 0, -\frac{1}{21}\sqrt{\frac{\pi}{5}}(v_1 - iv_2)(2v_1^2 + 5iv_1v_2 + 7v_2^2 + 3v_3^2), \frac{1}{7}\sqrt{\frac{\pi}{5}}(v_1 - iv_2)^2v_3,\right.$$
$$\left.\frac{1}{21}\sqrt{\frac{\pi}{5}}(iv_1 + v_2)(7v_1^2 - 5iv_1v_2 + 2v_2^2 + 3v_3^2), -\frac{2}{7}\sqrt{\frac{\pi}{5}}(v_1 - iv_2)^2v_3\right). \tag{B20}$$

In the above equations, we have listed by the components order 11, 12, 13, 22, 23, and 33 within a Cartesian coordinate. The position and velocity components mean $\vec{r} = (x_1, x_2, x_3)$, $\vec{v}_p = (v_1, v_2, v_3)$. And more we have

$$P_n^{\frac{1}{2}}Q^{ij} = \frac{3(m_1 - m_2)}{r}(n^iv_p^j + v_p^in^j - \dot{r}n^in^j), \tag{B21}$$

$$P_v^{\frac{1}{2}}Q^{ij} = (m_1 - m_2)\left(\frac{n^in^j}{r} - 2v_p^iv_p^j\right), \tag{B22}$$

$$P_0Q^{ij} = \frac{1}{3}\left\{\left[3(1 - 3\eta)v_p^2 - 2\frac{(2 - 3\eta)}{r}\right]v_p^iv_p^j + \frac{2}{r}\dot{r}(5 + 3\eta)(n^iv_p^j + v_p^in^j) + \left[3(1 - 3\eta)\dot{r}^2 - (10 + 3\eta)v_p^2 + \frac{29}{r}\right]\frac{n^in^j}{r}\right\}, \tag{B23}$$

$$P_{nn}Q^{ij} = \frac{1 - 3\eta}{3r}\left[\left(3v_p^2 - 15\dot{r}^2 + \frac{7}{r}\right)n^in^j + 15\dot{r}(n^iv_p^j + v_p^in^j) - 14v_p^iv_p^j\right], \tag{B24}$$

$$P_{nv}Q^{ij} = \frac{1 - 3\eta}{3r}[12\dot{r}n^in^j - 16(n^iv_p^j + v_p^in^j)], \tag{B25}$$

$$P_{vv}Q^{ij} = \frac{1 - 3\eta}{3}\left(6v_p^iv_p^j - \frac{2}{r}n^in^j\right), \tag{B26}$$

$$P_n^{\frac{3}{2}}Q^{ij} = \frac{(m_1 - m_2)}{12r}\left\{(n^iv_p^j + v_p^in^j)\left[\dot{r}^2(63 + 54\eta) - \frac{128 - 36\eta}{r} + v_p^2(33 - 18\eta)\right]\right.$$
$$\left. + n^in^j\dot{r}\left[\dot{r}^2(15 - 90\eta) - v_p^2(63 - 54\eta) + \frac{242 - 24\eta}{r}\right] - \dot{r}v_p^iv_p^j(186 + 24\eta)\right\}, \tag{B27}$$

$$P_v^{\frac{3}{2}}Q^{ij} = (m_1 - m_2)\left\{\frac{1}{2}v_p^iv_p^j\left[\frac{3 - 8\eta}{r} - 2v_p^2(1 - 5\eta)\right] - \frac{n^iv^j + v_p^in^j}{2r}\dot{r}(7 + 4\eta)\right.$$
$$\left. - \frac{n^in^j}{r}\left[\frac{3}{4}(1 - 2\eta)\dot{r}^2 + \frac{1}{3}\frac{26 - 3\eta}{r} - \frac{1}{4}(7 - 2\eta)v_p^2\right]\right\}, \tag{B28}$$

$$P^{\frac{3}{2}}_{nnn}Q^{ij} = \frac{(m_1-m_2)(1-2\eta)}{r}\left[\frac{5}{4}\left(3v_p^2-7\dot{r}^2+\frac{6}{r}\right)\dot{r}n^in^j-\frac{17}{2}\dot{r}v_p^iv_p^j-\left(21v_p^2-105\dot{r}^2+\frac{44}{r}\right)\frac{n^iv_p^j+v_p^in^j}{12}\right], \tag{B29}$$

$$P^{\frac{3}{2}}_{nnv}Q^{ij} = \frac{(m_1-m_2)(1-2\eta)}{4r}\left[58v_p^iv_p^j+\left(45\dot{r}^2-9v_p^2-\frac{28}{r}\right)n^in^j-54\dot{r}(n^iv_p^j+v_p^in^j)\right], \tag{B30}$$

$$P^{\frac{3}{2}}_{nvv}Q^{ij} = \frac{3(m_1-m_2)(1-2\eta)}{2r}(5(n^iv_p^j+v_p^in^j)-3\dot{r}n^in^j), \tag{B31}$$

$$P^{\frac{3}{2}}_{vvv}Q^{ij} = \frac{(m_1-m_2)(1-2\eta)}{2}\left(\frac{n^in^j}{r}-4v_p^iv_p^j\right). \tag{B32}$$

APPENDIX C: POST-NEWTONIAN ENERGY FLUX FOR AN ECCENTRIC BINARY

In this Appendix section, we show the post-Newtonian energy flux for an eccentric binary. Following [34] for the circular part, we can combine the results involved in SEOBNRv1 [14,34,88] to get

$$\begin{aligned}
-\left.\frac{dE}{dt}\right|_{(C)} &= \frac{32}{5}\eta^2x^5\left[1-\frac{1247+980\eta}{336}x+4\pi x^{3/2}+\left(-\frac{44711}{9072}+\frac{9271\eta}{504}+\frac{65\eta^2}{18}\right)x^2-\left(\frac{8191}{672}+\frac{583\eta}{24}\right)\pi x^{5/2}\right.\\
&+\left(\frac{6643739519}{69854400}-\frac{1712\gamma_E}{105}+\frac{16\pi^2}{3}-\frac{134543\eta}{7776}+\frac{41\pi^2\eta}{48}-\frac{94403\eta^2}{3024}-\frac{775\eta^3}{324}-\frac{856\log(16)}{105}-\frac{856\log(x)}{105}\right)x^3\\
&+\left(-\frac{16285}{504}+\frac{214745\eta}{1728}+\frac{27755\eta^2}{432}\right)\pi x^{7/2}\\
&+\left(-\frac{23971119313}{93139200}+\frac{856\gamma_E}{35}-8\pi^2-\frac{59292668653\eta}{838252800}+5a_0\eta+\frac{856\gamma\eta}{315}+\frac{31495\pi^2\eta}{8064}-\frac{54732199\eta^2}{93312}+\frac{3157\pi^2\eta^2}{144}\right.\\
&\left.+\frac{18929389\eta^3}{435456}+\frac{97\eta^4}{3888}+\frac{428\log(16)}{35}+\frac{428}{315}\eta\log(16)+\frac{428\log(x)}{35}+\frac{47468}{315}\eta\log(x)\right)x^4\\
&+\left(-\frac{80213}{768}+\frac{51438847\eta}{48384}-\frac{205\pi^2\eta}{6}-\frac{42745411\eta^2}{145152}-\frac{4199\eta^3}{576}\right)\pi x^{9/2}\\
&+\left(-\frac{121423329103}{82790400}+\frac{5778\gamma_E}{35}-54\pi^2+\frac{4820443583363\eta}{1257379200}-\frac{3715a_0\eta}{336}+6a_1\eta-\frac{4066\gamma_E\eta}{35}-\frac{31869941\pi^2\eta}{435456}\right.\\
&-\frac{2006716046219\eta^2}{3353011200}-\frac{55a_0\eta^2}{4}+\frac{214\gamma_E\eta^2}{105}+\frac{406321\pi^2\eta^2}{48384}+\frac{2683003625\eta^3}{3359232}-\frac{100819\pi^2\eta^3}{3456}-\frac{192478799\eta^4}{5225472}\\
&+\frac{33925\eta^5}{186624}+\frac{2889\log(16)}{35}-\frac{2033}{35}\eta\log(16)+\frac{107}{105}\eta^2\log(16)+\frac{2889\log(x)}{35}\\
&\left.-\frac{391669}{315}\eta\log(x)-\frac{122981}{105}\eta^2\log(x)\right)x^5+\left(-\frac{623565}{1792}-\frac{235274549\eta}{241920}+20a_0\eta+\frac{852595\pi^2\eta}{16128}\right.\\
&\left.-\frac{187219705\eta^2}{32256}+\frac{12915\pi^2\eta^2}{64}+\frac{503913815\eta^3}{870912}-\frac{24065\eta^4}{3456}+\frac{1792}{3}\eta\log(x)\right)\pi x^{11/2}\\
&+\left(-\frac{1216355221}{206976}+\frac{4815\gamma_E}{7}-225\pi^2+\frac{45811843687349\eta}{1149603840}+\frac{170515a_0\eta}{18144}-\frac{743a_1\eta}{56}+7a_2\eta+a_3\eta\right.\\
&-\frac{737123\gamma_E\eta}{189}-\frac{84643435883\pi^2\eta}{670602240}+\frac{8774}{63}\gamma_E\pi^2\eta-\frac{410\pi^4\eta}{9}-\frac{37516325949517\eta^2}{603542016}+\frac{68305a_0\eta^2}{2016}-\frac{33a_1\eta^2}{2}\\
&\left.+\frac{6634\gamma_E\eta^2}{63}+\frac{23084972185\pi^2\eta^2}{5225472}-\frac{92455\pi^4\eta^2}{1152}+\frac{6069288163291\eta^3}{2586608640}+\frac{295a_0\eta^3}{18}+\frac{107\gamma_E\eta^3}{243}-\frac{114930545\pi^2\eta^3}{1741824}\right.
\end{aligned}$$

$$
\begin{aligned}
&-\frac{145089945295\eta^4}{282175488}+\frac{141655\pi^2\eta^4}{7776}+\frac{6942085\eta^5}{497664}+\frac{196175\eta^6}{3359232}+\frac{4815\log(16)}{14}-\frac{737123}{378}\eta\log(16)\\
&+\frac{4387}{63}\pi^2\eta\log(16)+\frac{3317}{63}\eta^2\log(16)+\frac{107}{486}\eta^3\log(16)+\frac{4815\log(x)}{14}+\frac{13185899\eta\log(x)}{59535}+7a_3\eta\log(x)\\
&+\frac{4387}{63}\pi^2\eta\log(x)+\frac{963937}{189}\eta^2\log(x)+\frac{6279367\eta^3\log(x)}{2430}\Big)x^6+\left(-2\chi_S-\frac{3}{4}\sqrt{1-4\eta}\chi_A\right)x^{3/2}\\
&+\left[\left(-\frac{9}{4}+\frac{136}{9}\eta\right)\chi_S+\left(-\frac{23}{16}+\frac{157}{36}\eta\right)\sqrt{1-4\eta}\chi_A\right]x^{5/2}+\left(-8\pi\chi_S-\frac{17}{6}\pi\sqrt{1-4\eta}\chi_A\right)x^3\\
&+\left(\left(\frac{476645}{13608}+\frac{3086}{189}\eta-\frac{1405}{27}\eta^2\right)\chi_S+\left(\frac{180955}{27216}+\frac{625}{378}\eta-\frac{1117}{108}\eta^2\right)\sqrt{1-4\eta}\chi_A\right)x^{7/2}\Big],
\end{aligned}
\tag{C1}
$$

with $a_0=153.8803$, $a_2=-55.13$, $a_2=588$, $a_3=-1144$. These a values are taken from [34,88]. Here, $x\equiv\sqrt{v}$. The PN results for an elliptic orbit read [60,61]

$$
\begin{aligned}
-\left.\frac{dE}{dt}\right|_{\rm Elip}=&\frac{8}{15}\frac{M^4\eta^2}{r^4}\Big[12v^2-11\dot r^2+\frac{1}{28}\Big(-2\dot r^2v^2(1487-1392\eta)+v^4(785-852\eta)+3\dot r^4(687-620\eta)\\
&+\frac{8M\dot r^2(367-15\eta)}{r}+\frac{16M^2(1-4\eta)}{r^2}-\frac{160Mv^2(17-\eta)}{r}\Big)\\
&+\frac{1}{756}\Big(-\frac{24M^3(253-1026\eta+56\eta^2)}{r^3}-\frac{36Mv^4(4446-5237\eta+1393\eta^2)}{r}\\
&+\frac{108M\dot r^2v^2(4987-8513\eta+2165\eta^2)}{r}+\frac{M^2v^2(281473+81828\eta+4368\eta^2)}{r^2}+18v^6(1692-5497\eta+4430\eta^2)\\
&-\frac{3M^2\dot r^2(106319+9798\eta+5376\eta^2)}{r^2}-54\dot r^2v^4(1719-10278\eta+6292\eta^2)\\
&+54\dot r^4v^2(2018-15207\eta+7572\eta^2)-18\dot r^6(2501-20234\eta+8404\eta^2)-\frac{12M\dot r^4(33510-60971\eta+14290\eta^2)}{r}\Big)\Big]\\
&+\frac{8}{15}\frac{M^5\eta^2}{r^5}(\hat n\times\vec v)\cdot\Big[(\vec\chi_S+\sqrt{1-4\eta}\vec\chi_A)\Big(27\dot r^2-37v^2-12\frac{M}{r}\Big)+4\eta\vec\chi_S\Big(12\dot r^2-3v^2+8\frac{M}{r}\Big)\Big]\\
&+\frac{8}{15}\frac{M^6\eta^3}{r^6}[3(\chi_S^2-\chi_A^2)(47v^2-55\dot r^2)-3((\hat n\cdot\vec\chi_S)^2+(\hat n\cdot\vec\chi_A)^2)(168v^2-269\dot r^2)+71((\vec v\cdot\vec\chi_S)^2+(\vec v\cdot\vec\chi_A)^2)\\
&-342\dot r[(\vec v\cdot\vec\chi_S)(\hat n\cdot\vec\chi_S)-(\vec v\cdot\vec\chi_A)(\hat n\cdot\vec\chi_A)]],
\end{aligned}
\tag{C2}
$$

where the PN order for the nonspin part and spin-spin interaction part is second, but the PN order for the spin-orbit interaction part is only 1.5.

[1] B. P. Abbott *et al.* (Virgo, LIGO Scientific Collaborations), Phys. Rev. Lett. **116**, 061102 (2016).
[2] B. P. Abbott *et al.* (Virgo, LIGO Scientific Collaborations), Phys. Rev. Lett. **116**, 241103 (2016).
[3] B. P. Abbott *et al.* (LIGO Scientific and Virgo Collaborations), Phys. Rev. Lett. **118**, 221101 (2017).
[4] Z. Cao, Sci. China Phys. Mech. Astron. **59**, 110431 (2016).
[5] A. Taracchini, A. Buonanno, Y. Pan, T. Hinderer, M. Boyle, D. A. Hemberger, L. E. Kidder, G. Lovelace, A. H. Mroué, H. P. Pfeiffer *et al.*, Phys. Rev. D **89**, 061502 (2014).
[6] B. P. Abbott *et al.* (LIGO Scientific Collaboration and Virgo Collaboration), Phys. Rev. Lett. **116**, 241102 (2016).
[7] A. Buonanno, Y. Pan, J. G. Baker, J. Centrella, B. J. Kelly, S. T. McWilliams, and J. R. van Meter, Phys. Rev. D **76**, 104049 (2007).
[8] M. Pürrer, Phys. Rev. D **93**, 064041 (2016).
[9] S. Husa, S. Khan, M. Hannam, M. Pürrer, F. Ohme, X. J. Forteza, and A. Bohé, Phys. Rev. D **93**, 044006 (2016).
[10] S. Khan, S. Husa, M. Hannam, F. Ohme, M. Pürrer, X. J. Forteza, and A. Bohé, Phys. Rev. D **93**, 044007 (2016).

[11] T. Chu, H. Fong, P. Kumar, H. P. Pfeiffer, M. Boyle, D. A. Hemberger, L. E. Kidder, M. A. Scheel, and B. Szilagyi, Classical Quantum Gravity **33**, 165001 (2016).
[12] P. Kumar, T. Chu, H. Fong, H. P. Pfeiffer, M. Boyle, D. A. Hemberger, L. E. Kidder, M. A. Scheel, and B. Szilagyi, Phys. Rev. D **93**, 104050 (2016).
[13] Y. Pan, A. Buonanno, A. Taracchini, L. E. Kidder, A. H. Mroué, H. P. Pfeiffer, M. A. Scheel, and B. Szilágyi, Phys. Rev. D **89**, 084006 (2014).
[14] Z. Cao and W.-B. Han, Classical Quantum Gravity **33**, 155011 (2016).
[15] C. O. Lousto and Y. Zlochower, Phys. Rev. Lett. **106**, 041101 (2011).
[16] D. Bini and T. Damour, Phys. Rev. D **86**, 124012 (2012).
[17] F.-L. Julié and N. Deruelle, Phys. Rev. D **95**, 124054 (2017).
[18] N. Yunes, K. Yagi, and F. Pretorius, Phys. Rev. D **94**, 084002 (2016).
[19] P. C. Peters, Phys. Rev. **136**, B1224 (1964).
[20] J. Strader, L. Chomiuk, T. J. Maccarone, J. C. Miller-Jones, and A. C. Seth, Nature (London) **490**, 71 (2012).
[21] F. Antonini, S. Chatterjee, C. L. Rodriguez, M. Morscher, B. Pattabiraman, V. Kalogera, and F. A. Rasio, Astrophys. J. **816**, 65 (2016).
[22] J. Samsing, M. MacLeod, and E. Ramirez-Ruiz, Astrophys. J. **784**, 71 (2014).
[23] J. H. VanLandingham, M. C. Miller, D. P. Hamilton, and D. C. Richardson, Astrophys. J. **828**, 77 (2016).
[24] P. Amaro-Seoane, S. Aoudia, S. Babak, P. Binetruy, E. Berti, A. Bohe, C. Caprini, M. Colpi, N. J. Cornish, K. Danzmann *et al.*, Classical Quantum Gravity **29**, 124016 (2012).
[25] P. Bender, A. Brillet, I. Ciufolini, A. Cruise, C. Cutler, K. Danzmann, W. Folkner, J. Hough, P. McNamara, M. Peterseim *et al.*, LISA pre-phase A report (1998).
[26] H. Audley, S. Babak, J. Baker, E. Barausse, P. Bender, E. Berti, P. Binetruy, M. Born, D. Bortoluzzi, J. Camp *et al.*, arXiv:1702.00786.
[27] X. Gong, S. Xu, S. Bai, Z. Cao, G. Chen, Y. Chen, X. He, G. Heinzel, Y.-K. Lau, C. Liu *et al.*, Classical Quantum Gravity **28**, 094012 (2011).
[28] J. Luo, L.-S. Chen, H.-Z. Duan, Y.-G. Gong, S. Hu, J. Ji, Q. Liu, J. Mei, V. Milyukov, M. Sazhin *et al.*, Classical Quantum Gravity **33**, 035010 (2016).
[29] D. Hils and P. L. Bender, Astrophys. J. **445**, L7 (1995).
[30] M. Shibata, Phys. Rev. D **50**, 6297 (1994).
[31] N. Yunes, K. G. Arun, E. Berti, and C. M. Will, Phys. Rev. D **80**, 084001 (2009).
[32] E. A. Huerta, P. Kumar, S. T. McWilliams, R. O'Shaughnessy, and N. Yunes, Phys. Rev. D **90**, 084016 (2014).
[33] B. Sun, Z. Cao, Y. Wang, and H.-C. Yeh, Phys. Rev. D **92**, 044034 (2015).
[34] E. A. Huerta, P. Kumar, B. Agarwal, D. George, H.-Y. Schive, H. P. Pfeiffer, R. Haas, W. Ren, T. Chu, M. Boyle *et al.*, Phys. Rev. D **95**, 024038 (2017).
[35] U. Sperhake, E. Berti, V. Cardoso, J. A. González, B. Brügmann, and M. Ansorg, Phys. Rev. D **78**, 064069 (2008).
[36] I. Hinder, F. Herrmann, P. Laguna, and D. Shoemaker, Phys. Rev. D **82**, 024033 (2010).
[37] R. Gold and B. Brügmann, Phys. Rev. D **88**, 064051 (2013).
[38] W.-B. Han, Int. J. Mod. Phys. D **23**, 1450064 (2014).
[39] W.-B. Han and Z. Cao, Phys. Rev. D **84**, 044014 (2011).
[40] M. Sasaki and H. Tagoshi, Living Rev. Relativ. **6**, 6 (2003).
[41] E. Forseth, C. R. Evans, and S. Hopper, Phys. Rev. D **93**, 064058 (2016).
[42] S. Drasco and S. A. Hughes, Phys. Rev. D **73**, 024027 (2006).
[43] T. Apostolatos, D. Kennefick, A. Ori, and E. Poisson, Phys. Rev. D **47**, 5376 (1993).
[44] D. Kennefick, Phys. Rev. D **58**, 064012 (1998).
[45] E. E. Flanagan and T. Hinderer, Phys. Rev. Lett. **109**, 071102 (2012).
[46] C. P. L. Berry, R. H. Cole, P. Cañizares, and J. R. Gair, Phys. Rev. D **94**, 124042 (2016).
[47] A. G. Lewis, A. Zimmerman, and H. P. Pfeiffer, Classical Quantum Gravity **34**, 124001 (2017).
[48] N. Yunes, A. Buonanno, S. A. Hughes, M. C. Miller, and Y. Pan, Phys. Rev. Lett. **104**, 091102 (2010).
[49] H. Goldstein, C. Poole, and J. Safko, *Classical Mechanics* (Addison Wesley, Reading, Massachusetts, 2001).
[50] A. Buonanno and T. Damour, Phys. Rev. D **59**, 084006 (1999).
[51] A. Taracchini, Y. Pan, A. Buonanno, E. Barausse, M. Boyle, T. Chu, G. Lovelace, H. P. Pfeiffer, and M. A. Scheel, Phys. Rev. D **86**, 024011 (2012).
[52] B. P. Abbott *et al.* (LIGO Scientific Collaboration and Virgo Collaboration), Phys. Rev. X **6**, 041014 (2016).
[53] S. Babak, A. Taracchini, and A. Buonanno, Phys. Rev. D **95**, 024010 (2017).
[54] E. Barausse, E. Racine, and A. Buonanno, Phys. Rev. D **80**, 104025 (2009).
[55] E. Barausse and A. Buonanno, Phys. Rev. D **81**, 084024 (2010).
[56] E. Barausse and A. Buonanno, Phys. Rev. D **84**, 104027 (2011).
[57] S. Bai, Z. Cao, W.-B. Han, C.-Y. Lin, H.-J. Yo, and J.-P. Yu, J. Phys. Conf. Ser. **330**, 012016 (2011).
[58] Y. Pan, A. Buonanno, M. Boyle, L. T. Buchman, L. E. Kidder, H. P. Pfeiffer, and M. A. Scheel, Phys. Rev. D **84**, 124052 (2011).
[59] Y. Pan, A. Buonanno, R. Fujita, E. Racine, and H. Tagoshi, Phys. Rev. D **83**, 064003 (2011).
[60] C. M. Will and A. G. Wiseman, Phys. Rev. D **54**, 4813 (1996).
[61] L. E. Kidder, Phys. Rev. D **52**, 821 (1995).
[62] L. Blanchet, G. Faye, B. R. Iyer, and S. Sinha, Classical Quantum Gravity **25**, 165003 (2008).
[63] LIGO Scientific Collaboration, http://software.ligo.org/docs/lalsuite/lalsimulation.
[64] B. Brügmann, J. A. González, M. Hannam, S. Husa, U. Sperhake, and W. Tichy, Phys. Rev. D **77**, 024027 (2008).
[65] D. A. Nichols, Phys. Rev. D **95**, 084048 (2017).
[66] A. Buonanno, Y. Chen, and T. Damour, Phys. Rev. D **74**, 104005 (2006).
[67] Y. Pan, A. Buonanno, A. Taracchini, L. E. Kidder, A. H. Mroué, H. P. Pfeiffer, M. A. Scheel, and B. Szilágyi, Phys. Rev. D **89**, 084006 (2014).
[68] E. Barausse and L. Rezzolla, Astrophys. J. Lett. **704**, L40 (2009).
[69] W. Tichy and P. Marronetti, Phys. Rev. D **78**, 081501 (2008).

[70] Z. Cao, L.-F. Li, and Y. Wang, Phys. Rev. D **90**, 062003 (2014).
[71] LIGO Open Science Center (LOSC) Collaboration, https://losc.ligo.org/events/GW150914/.
[72] F. Messina and A. Nagar, Phys. Rev. D **95**, 124001 (2017).
[73] T. W. Baumgarte and S. L. Shapiro, *Numerical Relativity: Solving Einstein's Equations on the Computer* (Cambridge University Press, Cambridge, England, 2010).
[74] H. P. Pfeiffer, D. A. Brown, L. E. Kidder, L. Lindblom, G. Lovelace, and M. A. Scheel, Classical Quantum Gravity **24**, S59 (2007).
[75] A. H. Mroué, H. P. Pfeiffer, L. E. Kidder, and S. A. Teukolsky, Phys. Rev. D **82**, 124016 (2010).
[76] Caltech-Cornell-CITA Collaboration, Binary Black Hole Simulation Results, http://www.black-holes.org/waveforms.
[77] L. T. Buchman, H. P. Pfeiffer, M. A. Scheel, and B. Szilágyi, Phys. Rev. D **86**, 084033 (2012).
[78] Z. Cao, Phys. Rev. D **91**, 044033 (2015).
[79] J. M. Miller and E. Schnetter, Classical Quantum Gravity **34**, 015003 (2017).
[80] L. E. Kidder, S. E. Field, F. Foucart, E. Schnetter, S. A. Teukolsky, A. Bohn, N. Deppe, P. Diener, F. Hbert, J. Lippuner *et al.*, J. Comput. Phys. **335**, 84 (2017).
[81] P. Amaro-Seoane, J. R. Gair, M. Freitag, M. C. Miller, I. Mandel, C. J. Cutler, and S. Babak, Classical Quantum Gravity **24**, R113 (2007).
[82] L. Lindblom, B. J. Owen, and D. A. Brown, Phys. Rev. D **78**, 124020 (2008).
[83] L. Lindblom, Phys. Rev. D **80**, 042005 (2009).
[84] L. Lindblom, Phys. Rev. D **80**, 064019 (2009).
[85] L. Lindblom, J. G. Baker, and B. J. Owen, Phys. Rev. D **82**, 084020 (2010).
[86] L. Lindblom and C. Cutler, Phys. Rev. D **94**, 124030 (2016).
[87] Y. Pan, A. Buonanno, L. T. Buchman, T. Chu, L. E. Kidder, H. P. Pfeiffer, and M. A. Scheel, Phys. Rev. D **81**, 084041 (2010).
[88] E. Barausse, A. Buonanno, and A. Le Tiec, Phys. Rev. D **85**, 064010 (2012).